Ph.D. Dissertation of Engineering

Growth control of transition metal chalcogenides by metal precursors and promoters

금속 전구체와 성장 촉진제를 통한 전이금속 칼코겐화물의 성장 제어

August 2023

Graduate School of Engineering
Seoul National University
Materials Science and Engineering

Yeonjoon Jung

Growth control of transition metal chalcogenides by metal precursors and promoters

Advisor: Prof. Gwan-Hyoung Lee

Submitting a Ph.D. Dissertation of
Engineering

August 2023

Graduate School of Engineering
Seoul National University
Materials Science and Engineering

Yeonjoon Jung

Confirming the Ph.D. Dissertation written by
Yeonjoon Jung
August 2023

Chair	Min Hyuk Park	(Seal)
Vice Chair	Gwan-Hyoung Lee	(Seal)
Examiner	Hyejin Jang	(Seal)
Examiner	Jihyun Kim	(Seal)
Examiner	Jangyup Son	(Seal)

Acknowledgements

가장 먼저 지도교수님이신 이관형 교수님께 감사의 말씀을 드립니다. 여러가지 연유로 제가 연구의 길을 걷는 것이 어려워졌을 때, 제가 무사히 연구를 마칠 수 있도록 아낌없는 지원과 조언으로 무사히 학위과정을 마칠 수 있게 지도해 주셔서 감사드립니다. 제가 많이 부족했음에도 불구하고 박사까지 이끌어 주신 감사함을 평생 잊지 않고 보답하며 살겠습니다.

또한, 바쁘신 중에도 심사를 맡아 주시고 논문을 개선할 수 있도록 도와주신 박민혁 교수님, 장혜진 교수님, 김지현 교수님, 손장엽 박사님 이상 모든 심사위원 분들께도 감사의 인사를 올립니다.

다음으로 낯설고 힘들었던 대학원 생활에서 연구실 동료로서, 친구로서 버틸 수 있도록 원동력을 주고, 연구에 대해 논의하며, 즐거운 대학원 추억을 만들어 남길 수 있게 도와준 권준영, 김한결, 류희제에게 고맙다고 전하고 싶습니다.

이외에도 많이 부족했던 저를 따라 연구 진행을 도와주었던 후배들을 비롯하여 연구에 많은 도움을 주었던 연구실 선후배에게도 감사드립니다.

마지막으로, 조금은 제멋대로였던 제가 학업을 계속하는데에 있어서 전폭적으로 지원해주고 믿어주신 아버지, 어머니 그리고 동생까지 사랑하는 우리 가족에게 이 논문과 학위의 공을 돌리고 싶습니다.

학위의 결실은 제가 받았지만, 이 학위에는 저를 위해 관심과 사랑을 주신 많은 분들의 도움이 담겨있다는 것을 항상 마음속에 간직하면서, 응원해주신 모든 분들께 다시 한 번 감사의 말씀을 올리며 마치도록 하겠습니다.

2023년 6월

정연준 올림

Abstract

Two-dimensional (2D) materials and their heterostructures are promising for next-generation optoelectronics, spintronics, valleytronics, and electronics. Despite recent progress in various growth studies of 2D materials, mechanical exfoliation of flakes is still the most common method to obtain high-quality 2D materials because precisely controlling material growth and synthesizing a single domain during the growth process of 2D materials, for the desired shape and quality, is challenging.

In this thesis, most of works are focused on the growth of 2D transition metal dichalcogenides materials to tailor their physical properties. Prior to introducing the detailed studies, brief general background about 2D materials properties and growth including importance of analyzing growth mechanisms are given in chapter 1. Then, to growth of desired transition metal dichalcogenides, three growth methods are described in chapter 2.

Here, I successfully modified and modulated the PL of MoS_2. Through PL imaging, I observed a gradual enhancement in PL intensity within the imaging area, resulting from repetitive light illumination. The point PL measurements provided quantitative evidence of approximately 7-fold enhancement in PL intensity. And the low-temperature PL and

XPS measurements show that tins enhancement has relationship with defect healing. So, this enhancement can be attributed to increased radiative recombination of excitons and defect healing facilitated by repetitive light illumination.

Also, I find that liquid phase tungsten oxide (WO_x), an intermediate phase produced during the growth process, facilitates the growth of multilayer WS_2. The intermediate WO_x with high oxygen ratio ($x>3$) becomes a liquid phase so that sulfur can be dissolved in liquid WO_x, resulting in nucleation of multilayer WS_2 on the WO_x surface. Then, the WS_2 grows laterally by squeezing out the liquid WO_x outward due to higher interface energies between WS_2 and WO_x. The grown multilayer WS_2 single crystals have various stacking orders of 2H and 3R, which is confirmed by second-harmonic generation (SHG) signals and photoluminescence (PL).

Finally, I report the nucleation and growth behaviors of monolayer MoS_2 by sulfurizing a faceted monoclinic MoO_2 crystal. The MoS_2 layers nucleated at the thickness steps of the MoO_2 crystal and grew epitaxially with crystalline correlation to the MoO_2 surface. The epitaxially grown MoS_2 layer expands outwardly on the SiO_2 substrate, resulting in a monolayer single-crystal film, despite multiple nucleations of MoS_2 layers on the MoO_2 surface owing to several thickness steps.

Although the photoluminescence of MoS_2 is quenched owing to efficient charge transfer between MoS_2 and metallic MoO_2, the MoS_2 stretched out to the SiO_2 substrate shows a high carrier mobility of (15 $cm^2V^{-1}s^{-1}$), indicating that a high-quality monolayer MoS_2 film can be grown using the MoO_2 crystal as a seed and precursor. Our work demonstrates a route to grow high-quality MoS_2 using a faceted MoO_2 crystal and provides a deeper understanding of the nucleation and growth of 2D materials on a step-like surface.

Our findings can provide a better understanding of growth in 2D materials, which can be applied to design a new growth method for 2D materials

Keyword: Two-dimensional materials, Transition metal chalcogenides, Growth mechanism, Chemical Vapor Deposition, Physical Vapor Deposition, Chalcogenization

Student Number: 2020-28958

Table of Contents

Chapter 1. Introduction

1.1 Properties of Transition Metal Chalcogenides

Structure of Transition metal chalcogenides

Transition metal chalcogenides are the most studied layered materials beyond graphene. They typically have the formula MX_2 and consist of a sandwich of two chalcogen atoms (X) centered on a transition metal(M) forming one atomic layer. Transition metal chalcogenides are composed of strong covalent bonding within the intralayer, but stacking vertically interlayer with relatively weak van der Waals forces. [1] This unique bonding structure makes it possible to reveal and exploit the layer-by-layer physicochemical properties of transition metal chalcogenides as layered materials. Transition metal chalcogenides have the same chemical formula of MX_2, but have several phases due to the difference in arrangement within three atoms thick. There is the 1H phase, which is in the form of a trigonal prismatic around the metal atom center, and the 1T phase, which has an octahedral coordination. In addition, the 1T' phase is representative, [2, 3] in which the chalcogen atom is also distorted by the distortion between adjacent metal atoms in the 1T phase.

In general, crystal structures with high periodicity such as 2H and 1T phases are thermodynamically stable and 1T' is metastable, but in certain situations, 1T' phase can be kept stable even at room temperature. In addition, phases such as 2H or 3R exist depending on the stacking order of transition metal chalcogenides between interlayers instead of within intralayers.[4, 5] The degree of freedom provided by the various crystal structures of transition metal chalcogenides shows a variety of properties despite the fact that the structure is simply composed of one metal atom and two chalcogen atoms, which has numerous potential applications in the next-generation nanoscale industry.

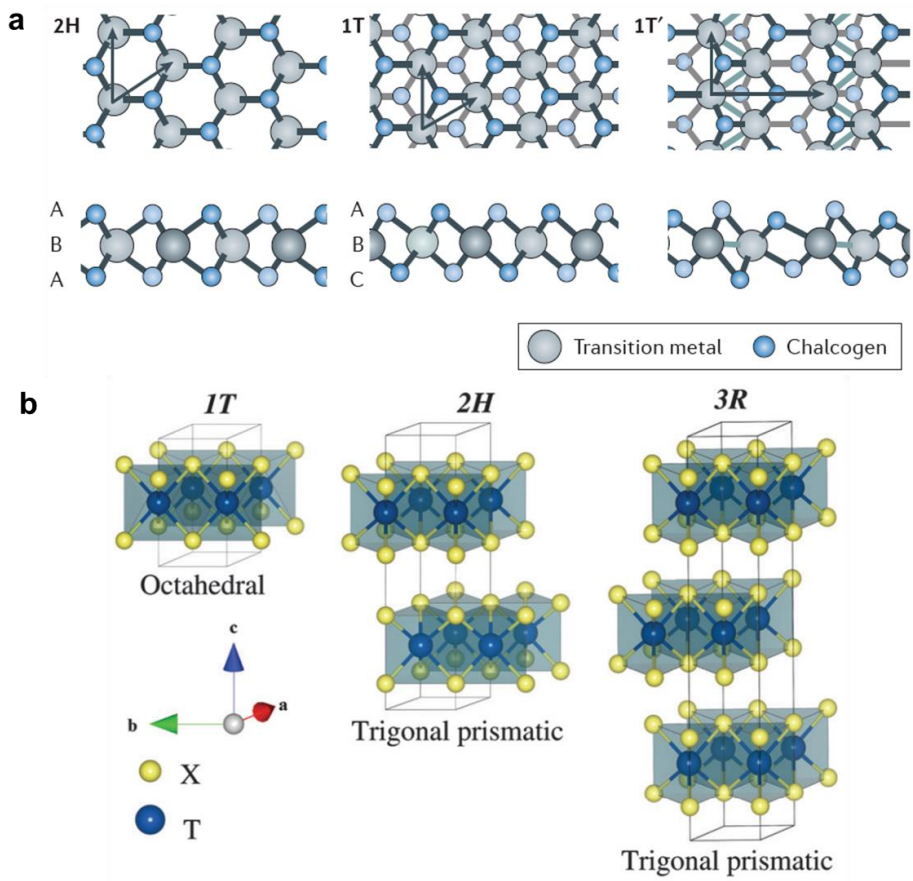

Figure 1.1 Structure of TMDCs. a) Atomic structure of single layers of transition metal dichalcogenides (TMDCs) in their trigonal prismatic (2H), distorted octahedral (1T), and dimerized (1T′) phases. Lattice vectors and the stacking of atomic planes are indicated. [6] b) Structural representation of 1T, 2H, and 3R TMDC polytypes together with their metal atom coordination. The numbers indicate the number of layers in the unit cell and the letters stand for trigonal, hexagonal, and rhombohedral, respectively. [7]

Band properties of Transition metal chalcogenides

The diversity of properties arising from the different structural phases and changes in chemical composition of transition metal chalcogenides shows the potential to diversify the band properties of transition metal chalcogenides and exploit a wide range of electrical and optoelectronic properties. These band properties range from metallic to semiconducting and beyond, and include charge density wave, superconducting, and topological properties. Typical and most widely studied transition metal chalcogenides are sulfur or selenium compounds with Mo and W as transition metal centers. These transition metal dichalcogenides have different band properties depending on the number of layers, and the peculiarity is that when only a three-atom-thick monolayer is present, the indirect band properties in the conventional bulk change to direct band properties at the K-K momentum. [8-10] This direct band characteristic implies that these two-dimensional semiconducting materials can be utilized not only for electrical but also optical properties. These transition metal chalcogenides show not only band characteristic changes with the number of layers, but also inequivalence at high symmetry points in the Brillouin zone, where the Valley degeneracy decay makes the transition metal chalcogenides selective to certain circularly polarized

light. This increased degree of freedom holds promise for valleytronics applications that utilize the valley selectivity within transition metal chalcogenides.

A special property exhibited by these monolayer transition metal chalcogenides is the spin splitting of electronic bands by spin-orbit coupling (SOC). The strong SOC of the two-dimensional transition metal chalcogenides collapses the spin degeneracy of the VBM and CBM. The spin splitting at the valence band maximum in monolayers has relatively large energies, ranging from 0.15 eV in MoS_2 to 0.46 eV in WSe_2 with heavier atoms.[11] In CBM, spin splitting occurs for the same reason, but the contribution of the orbital of the metal atom involved in CB is lower,[12] showing about an order of magnitude lower splitting compared to VB. The transition metal chalcogenide shows opposite spin splitting in the two K, K' of the Brillouin zone due to the time-reversal symmetry caused by the asymmetry of each atom at 3-fold as opposed to graphene at 6-fold. This unique spin-valley polarization [13] enables spintronic applications in transition metal chalcogenides without the need for any magnetic materials. [14, 15]

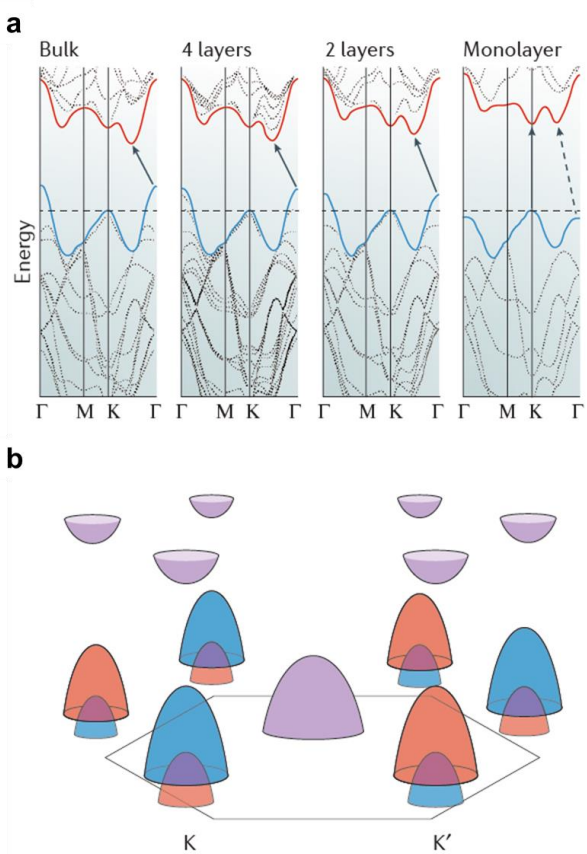

Figure 1.2 a) Evolution of the band structure of 2H-MoS_2 calculated for samples of decreasing thickness. b) Schematic representation of the band structure of monolayer 2H-MoS_2, showing the spin splitting of the bands at the K and K´ points on the corners of the Brillouin zone. Orange and blue colors indicate up-and- down spin polarization.

6

1.2 Fabrication method of Transition Metal Chalcogenides

Top-down method

The intrinsic inter- and intralayer anisotropy, as seen in the structure of transition metal chalcogenides described earlier, allows for the separation of several layers of thin nanosheets from bulk two-dimensional materials. [16] There are various ways to overcome these interlayer van der Waals forces. [1] First of all, as shown in Figure 1.3, micromechanical methods can be used to peel off the bulk two-dimensional material, induce interlayer distortion through compression to weaken the van der Waals force, or apply shear stress [17-19] to obtain single or multiple layers of two-dimensional material. For peel-off, the best known example is the scotch tape method. [20, 21]

Another method is exfoliation in a solvent. There are also physical methods (vibration and cavitation) [22-24] and chemical intercalation methods. [25-27] In the case of the physical method, the crystal is separated by applying vibration energy through sonication to the two-dimensional bulk material or forming a cavitation field through the control of fluid flow in the solvent and applying the

resulting force to the two-dimensional bulk material to obtain a thinner flake of transition metal chalcogenides.

Chemically exfoliated methods in solvent typically overcome interlayer van der Waals forces by inducing interlayer expansion through intercalation. The most commonly used intercalation materials are alkali metal cations with small electronegativity. The alkali metal cation is inserted into the interlayer of the two-dimensional TMD, causing orbital hybridization and charge transfer to the d-band of the transition metal chalcogenide. [28-30] To stabilize the change in charge distribution, a phase transition of the transition metal chalcogenide occurs, and the weakened interlayer distance is separated into independent layers by gas generation in a specific solvent medium.

In addition, there are methods such as etching, [31-36] which is not a peeling method that overcomes the van der Waals between interlayers, but a method that uses a laser or other destructive method to create a layer of the desired thickness in the bulk, starting from the most surface layer sequentially.

Although these various methods have been studied, the main disadvantage is that it is difficult to control the energy delivered for separation and destruction of layers, making it difficult to produce

two-dimensional materials with the desired size and number of layers. To overcome this disadvantage, many researchers have studied how to grow two-dimensional materials from the bottom up through a combination of atomic steps rather than from bulk materials.

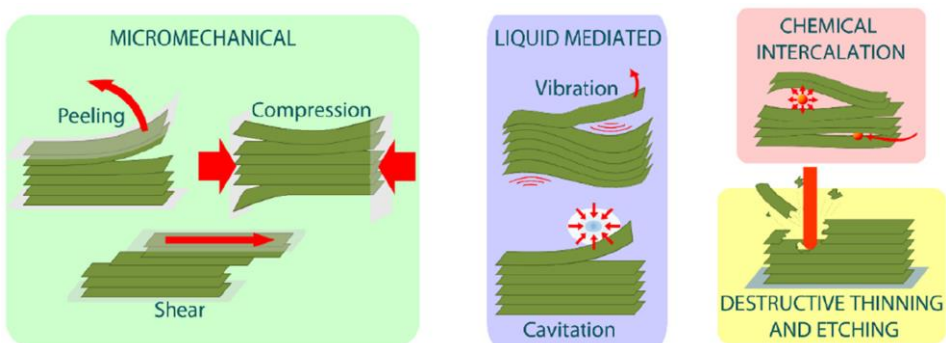

Figure 1.3 Representation of the forces used to exfoliate nanosheets in 'top-down' methods. [37]

Bottom-up synthesis

Unlike the top-down method, the bottom-up synthesis of two-dimensional transition metal chalcogenides proceeds through the reaction of a precursor(s) containing the elements of the transition metal chalcogenide. In general, the types of precursors involved in the synthesis of transition metal chalcogenides include solid, liquid, and gaseous phases and are accompanied by various types of chemical reactions. In theory, any material containing the elements of the target transition metal chalcogenide can be used as a precursor, but difficulties in controlling the energetics and reaction kinetics [38] limit the number of precursors that can be utilized in practice. As mentioned earlier, transition metal chalcogenides are anisotropic to energy in certain planes due to their unique layered structure. The inherent anisotropy of energy of the basal and edge planes in transition metal chalcogenides forces growth in the lateral direction in layered material growth, unlike conventional non-layered materials. [39] This is due to the absence of dangling bonds in the basal plane. [39] At the edge sites of relatively high-energy of layered materials, the unbalanced charge distribution formed by dangling bonds allows for the formation of continuous covalent bonding of atoms supplied from precursors. This anisotropy in growth enables the self-limited growth of atom thick

nanosheets in two-dimensional materials for scale-down to next-generation semiconductor materials.

Although many researchers have devised synthetic methods to grow various types of transition metal chalcogenides and elucidated their growth mechanisms, there is still much work to be done to provide a comprehensive description of all aspects of growth. In this article, I will discuss chemical vapor deposition, physical vapor deposition, and chalcogenization of metal precursor films as representative bottom-up growth methods.

Vapor Deposition

Vapor deposition is the most widely recognized material growth method for forming thin films on substrates. The chemical reaction of a precursor supplied in a gas phase chamber allows the target material to be grown on the substrate. There are many different variations of vapor deposition methods [40], but the basic process is similar regardless. [41, 42] As shown in Figure 1.4, a reactant (usually vapor) is introduced into the chamber through an inert carrier gas, [43, 44] which forms intermediate reactants or gaseous byproducts through a gas phase reaction, and then adsorbs on the substrate to cause nucleation and grain growth, or the reactant itself is adsorbed on the boundary layer

of the substrate and then directly diffuses to cause nucleation and grain growth of the target material. At this time, the gas phase reaction occurring in the chamber requires sufficient energy to overcome the activation energy, so a sufficiently high temperature is applied to the chamber or additional energy such as plasma is applied. In the vapor deposition method of transition metal chalcogenides, monomer units of transition metal chalcogenides are formed and then nanosheets are formed on the substrate. In the case of two-dimensional transition metal chalcogenides, there are many reports of atomic-thickness monolayer growth using vapor deposition. [45-47] The vapor deposition method has the advantage of fundamentally solving the problem of the dependence of the scale of the nanosheet [43, 48] on the properties of the starting material, which is the biggest drawback of the top-down method introduced earlier. Therefore, the vapor deposition method of two-dimensional transition metal chalcogenides remains a major challenge for future research to catch up with the quality obtained by the microexfoliation method from bulk crystals obtained by chemical vapor transport, etc. and to maintain reproducibility during the growth process through the control of various variables.

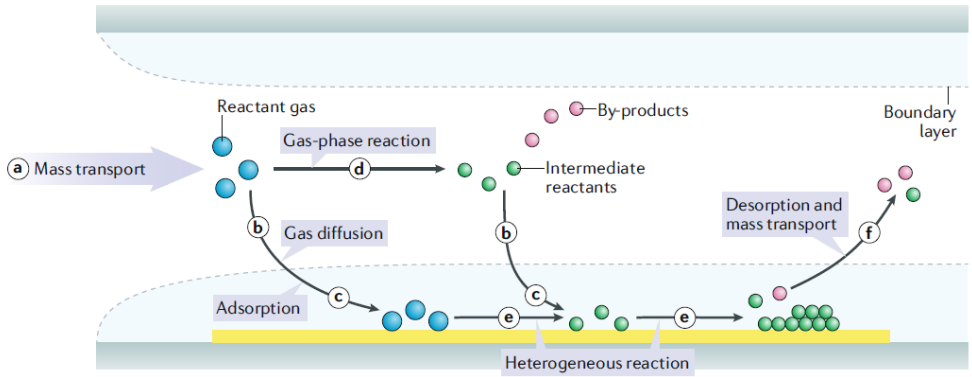

Figure 1.4 Schematic of general elementary steps of a typical CVD process. First, reactant gases (blue circles) are transported into the reactor (step a). Then, there are two possible routes for the reactant gases: directly diffusing through the boundary layer (step b) and adsorbing onto the substrate (step c); or forming intermediate reactants (green circles) and by-products (red circles) via the gas-phase reaction (step d) and being deposited onto the substrate by diffusion (step b) and adsorption (step c). Surface diffusion and heterogeneous reactions (step e) take place on the surface of substrate before the formation of thin films or coatings. Finally, by-products and unreacted species are desorbed from the surface and forced out of the reactor as exhausts (step f). CVD, chemical vapour deposition. [40]

Chalcogenization

Chalcogenization is an alternative to gas phase reactions. Gas-phase reactions suffer from low yields and low growth selectivity due to transport steps in the vapor deposition process. These are factors that reduce the reproducibility of the growth of transition metal chalcogenides. Chalcogenization is a method to overcome these problems and directly synthesize two-dimensional transition metal chalcogenides at targeted locations by directly chalcogenizing a substrate coated with a precursor containing a metal atom as one of the precursors. Unlike the previous vapor deposition method, this method does not force a path for gas diffusion after the gas-phase reaction, resulting in a high yield of transition metal chalcogenides and high growth selectivity that allows growth only at the desired location through pre-patterning of the precursor. The types of metal precursors used for this chalcogenization range from metal films to sources such as metal oxides and alloys. [49-56] However, in the case of this chalcogenization, the film thickness and crystal size of the transition metal chalcogenide grown by random nucleation and grain growth on the surface of the metal-containing film are random, and this plays a major role in reducing the uniformity of the film. As a result, the grain boundaries and defect density are high, and the grains

are often misaligned and cannot form a monolayer. [52] These structural features are manifested in the deterioration of the electro-optical properties of transition metal chalcogenides formed by chalcogenization of metal source-containing films compared to transition metal chalcogenides synthesized by conventional vapor deposition methods. Therefore, controlling the nucleation of these films and controlling the alignment of the growing grains remain the most important issues.

Figure 1.5 Chalcogenization (sulfurization/selenization) of pre-deposited (a) Mo or (b) MoO_3 thin film [57]

1.3 Analyze of growth mechanisms in two-dimensional materials

For practical applications of two-dimensional materials, it is not only important to synthesize two-dimensional transition metal chalcogenides with desired properties, but it is also crucial to increase the reproducibility of the process. In order to improve the reproducibility, it is necessary to understand the mechanism of growth by identifying the influence of different factors on the process. Therefore, it is essential to study the connection between the material growth theory of two-dimensional transition metal chalcogenides and the synthesis process of various methods. In this respect, single crystal materials offer the possibility to understand the nucleation and growth mechanisms and control the material properties.

Currently, several growth models have been proposed for two-dimensional materials. These include Layer-By-Layer, Layer-Over-Layer, Screw-Dislocation-Driven, [58-61] and Dendritic models. [62] For all condensed solid state materials, including two-dimensional materials, the degree of saturation of the reactant determines the growth model of the material. As shown in Figure 1.6, the concentration of reactants contributes to different growth models.

Layer-by-layer (LBL) growth is commonly observed in two-dimensional materials such as transition metal chalcogenides, including graphene. This is due to the intrinsic structural anisotropy of layered materials, which is difficult to overcome because the activation energy for nucleation of a new layer is higher than the activation energy for lateral growth of edge sites with dangling bonds. To overcome this difficulty, supersaturation conditions of the reactants are required so that the vertical growth of LBL growth can be dominant. In addition, screw-dislocation-driven growth, which has previously been shown in one-dimensional nanomaterials (nanotubes or nanochannels), has been confirmed to occur in two-dimensional materials at low supersaturation concentrations. Understanding this growth model goes beyond controlling the properties of two-dimensional transition metal chalcogenides, which appear in a single three-atom-thick layer, and allows for control of the number of layers and morphology, increasing the probability that certain crystals will be synthesized over others, leading to a broader range of applications for low-dimensional materials.

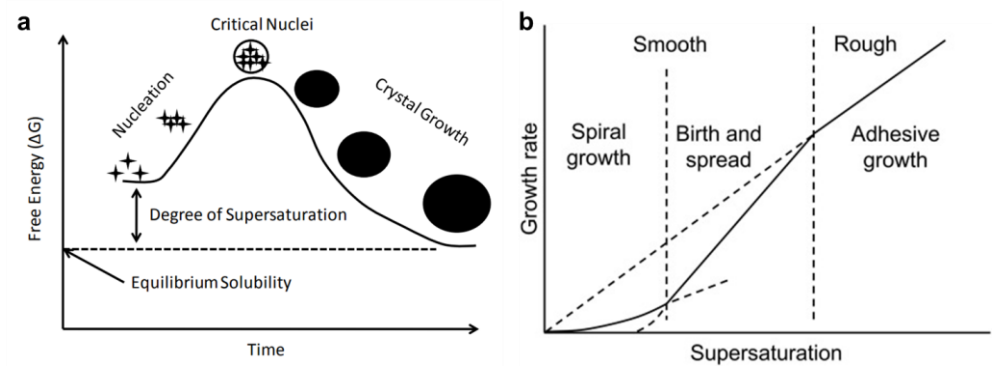

Figure 1.6 a) Schematic diagram illustrating the change in free energy during crystallization. [63] b) Mechanisms of growth as a function of supersaturation [64]

Chapter 2. Growth control of transition metal chalcogenides by metal precursors and promoters

2.1. Enhanced Photoluminescence and Defect Healing in Large-Scale MoS_2 via NaBr promoter-assisted growth

2.1.1. Introduction

Two-dimensional materials have attracted significant attention in recent years due to their unique properties and potential applications in various fields, including optoelectronics, [65-69] energy storage, [70-75] Among them, molybdenum disulfide (MoS_2), a transition metal dichalcogenide, has gained particular interest owing to its semiconducting nature and excellent optical properties. [76-78] However, the synthesis of large-scale MoS_2 with controlled quality remains a challenge. Conventional chemical vapor deposition (CVD) methods have been widely employed for MoS_2 synthesis; however, they are often limited by the high thermal stability of the precursor and the fundamental issues associated with chemical vapor deposition techniques. To overcome these limitations and achieve large-scale synthesis of high-quality MoS_2, the use of promoters has been explored.

In this study, I utilized a NaBr promoter in the synthesis process of MoS_2. The incorporation of the NaBr promoter enabled the

successful fabrication of MoS_2 with large sizes. The obtained films exhibited typical optical properties of MoS_2. Nevertheless, I investigated the optical properties of the synthesized MoS_2 through repeated light illumination. I observed a significant enhancement in the photoluminescence (PL) intensity across the entire spectrum upon continuous light illumination. This finding suggests that the optical properties of the MoS_2 via promoted grown can be modulated through light-induced effects. To gain insights into the origin of this enhanced PL, I performed low-temperature PL measurements. The results of the low-temperature PL measurements revealed distinct characteristics depending on the illumination conditions. Immediately after synthesis without any illumination, the low-temperature PL spectra exhibited a high ratio of trions and defect-bound excitons to neutral exciton. However, after sufficient illumination, the defect-bound exciton peak significantly decreased, accompanied by a decrease in the trion ratio. These observations indicate that the enhanced PL intensity is associated with the modification of defect-related states in the MoS_2 upon illumination. To further investigate the characteristics of the promoted-grown MoS_2 films and the role of defect healing, I conducted X-ray photoelectron spectroscopy (XPS) measurements. The analysis of the XPS spectra demonstrated the disappearance of

trap states formed by sulfur vacancies, leading to a lower Fermi level of the MoS_2 grains. Consequently, the binding energy of Mo and S exhibited a redshift. This result confirms the successful defect healing in the promoted-grown MoS_2, which can be achieved through light illumination.

2.1.2. Experimental procedure

PL imaging

To ensure specific excitation of the MoS_2 band, a short pass filter was installed in the path of the incident light in the microscope setup. This filter effectively blocked wavelengths that could lead to band excitation in MoS_2. Additionally, a long pass filter was placed in the path of the emitted light, after it passed through the sample and the dichroic mirror, and before reaching the CCD camera. This arrangement allowed us to eliminate any reflected light and focus solely on the PL emission. Figure 2.1 illustrates the modified microscope setup.

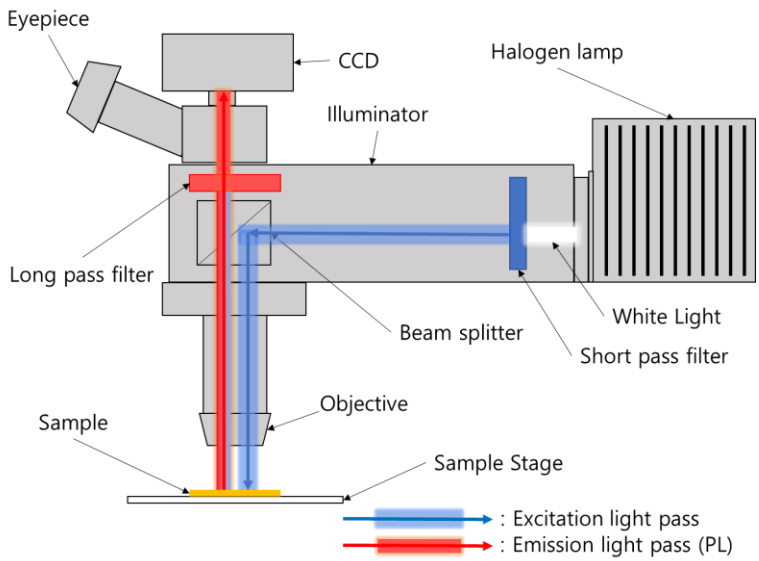

Figure 2.1 Customized PL imaging set-up using optical microscopy

CVD growth of MoS_2

Monolayer MoS_2 on SiO_2 (285 nm)/Si substrate was synthesized using an APCVD (atmospheric pressure CVD) system. Before the growth process, substrates (2.3×2.3 cm^2) were cleaned via sonication in acetone and isopropyl alcohol for 10 min each. Molybdenum trioxide powder (MoO_3, 3 mg, Sigma-Aldrich) and NaBr powder (3mg, Alfa-Aesar) mixture loaded quartz boat was heated to 750 °C at center of the furnace. Another quartz boat filled with sulfur powder (S, 180 mg, Sigma-Aldrich) was placed at 21 cm away from the center toward the upstream (temperature of sulfur is measured as 220 °C). The substrate was positioned upside-down on MoO_3 powder filled quartz boat. The temperature of furnace was ramping up to the reaction temperature of 750 °C with a ramping rate of 50 °C /min. Reaction maintained for 5 min with supplying Ar gas (300 sccm) to the substrate. After growth, the furnace was cooled naturally to 300 °C, followed by rapid cooling.

Raman Spectroscopy

The Raman intensity map image and spectra were acquired using Raman spectroscopy (LabRAM HR Evolution) with a 532 nm

laser. To minimize the damage to the sample from laser irradiation, a power of < 5 mW was used. As the laser spot size was ≈1 μm. The measurements were conducted at room temperature and low temperature(77K) using linkam stage.

XPS measurement

XPS spectra were collected in a PHI VERSAPROBE III SCANNING XPS MICROPROBE system using a monochromatic Al Kα X-ray source.

2.1.3. Results and Discussion

In order to investigate the photoluminescence (PL) imaging of MoS_2, I modified a microscope setup (See Methods for detail). Using PL imaging setup, I performed PL imaging of MoS_2 samples and observed intriguing behavior. Initially, in bright field (BF) image of MoS_2(Figure 2.2a), PL signal appeared relatively weak across the image, as shown in Figure 2.2b. However, through repetitive light illumination, I observed a gradual enhancement in the PL intensity within the imaging area. Figure 2.2c clearly demonstrates the progressive brightening of previously dark regions in the PL imaging.

To quantify the observed enhancement in PL intensity, I performed point PL measurements on each sample. The results, as depicted in Figure 2.2d, revealed an approximate 7-fold increase in PL intensity compared to non-enhanced MoS_2.

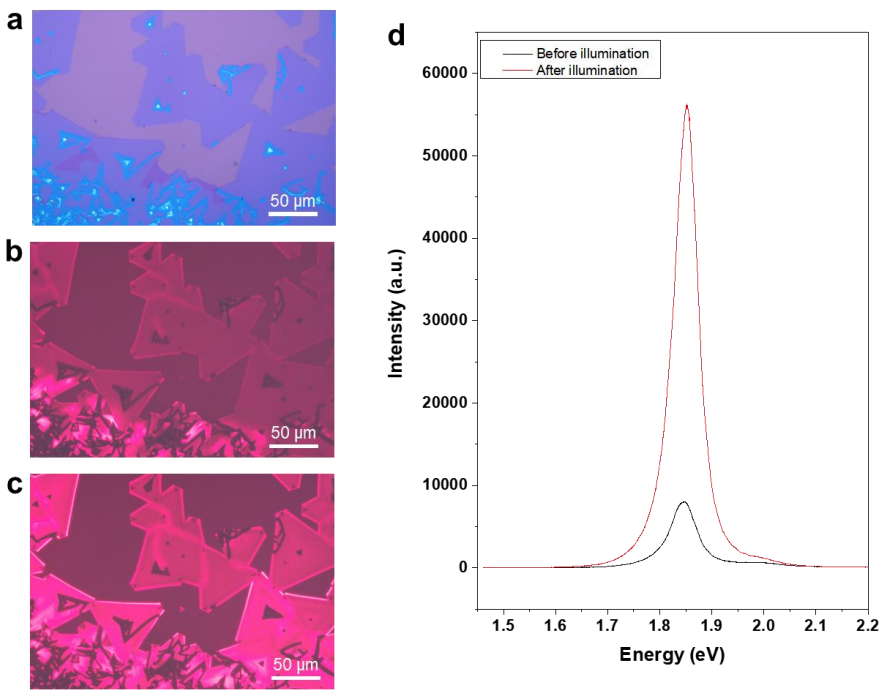

Figure 2.2 PL enhancement of MoS_2 by light illumination. (a) OM image of promoted grown MoS_2, (b) PL image of promoted grown MoS_2 (b) before and (c) after illumination. PL spectra before and after illumination.

To investigate the origin of photoluminescence (PL) in the synthesized MoS_2, I performed low-temperature PL measurements on three different types of CVD-grown MoS_2 samples: (Red) non-enhanced promoted grown MoS_2, (Black) fully enhanced promoted grown MoS_2, and (Blue) conventionally grown MoS_2. (Figure 2.3)

Our results revealed distinct PL characteristics among the three samples. In the PL spectra of sample (Red) and sample (Blue), a prominent peak corresponding to defect-bound excitons was observed. However, in sample (Black), the intensity of the defect-bound exciton peak was significantly reduced. This observation suggests that the use of a promoter during the growth process has a notable effect on the self-abandonment of defect-bound PL in MoS_2 (Figure 2.3 (red)).

To further analyze the PL peaks, I utilized the peak corresponding to the neutral exciton as a reference. The A-B spin-orbit splitting for all three types of samples was found to be approximately 170 meV, [79, 80] indicating similar spin-orbit coupling strength. However, for the defect-bound exciton peaks, two distinct peaks with energy differences of approximately 130 meV and 180 meV were observed. According to previous studies [81], the peak with a 130 meV energy difference is attributed to mono-sulfur vacancies, while the peak with a 180 meV energy difference is associated with di-sulfur

vacancies. [81] This discrepancy in peak energies suggests that the defect types differ between the two samples(Figure 2.3;Red and Blue).

The disparity in defect types can be attributed to the growth conditions and the influence of the promoter. According to the referenced studies, [82] he MoS_2 synthesized with a promoter under Mo-rich conditions exhibits a lower chemical potential of sulfur, which leads to a relatively lower formation energy for di-sulfur vacancies. [82] This condition favors the formation of di-sulfur vacancies rather than mono-sulfur vacancies, resulting in the observed peak energy difference of approximately 180 meV.

These findings highlight the role of the promoter in modulating the defect characteristics of MoS_2 during growth. The incorporation of a promoter under Mo-rich conditions can effectively enhance the formation of di-sulfur vacancies, leading to a higher density of defect-bound PL in MoS_2.

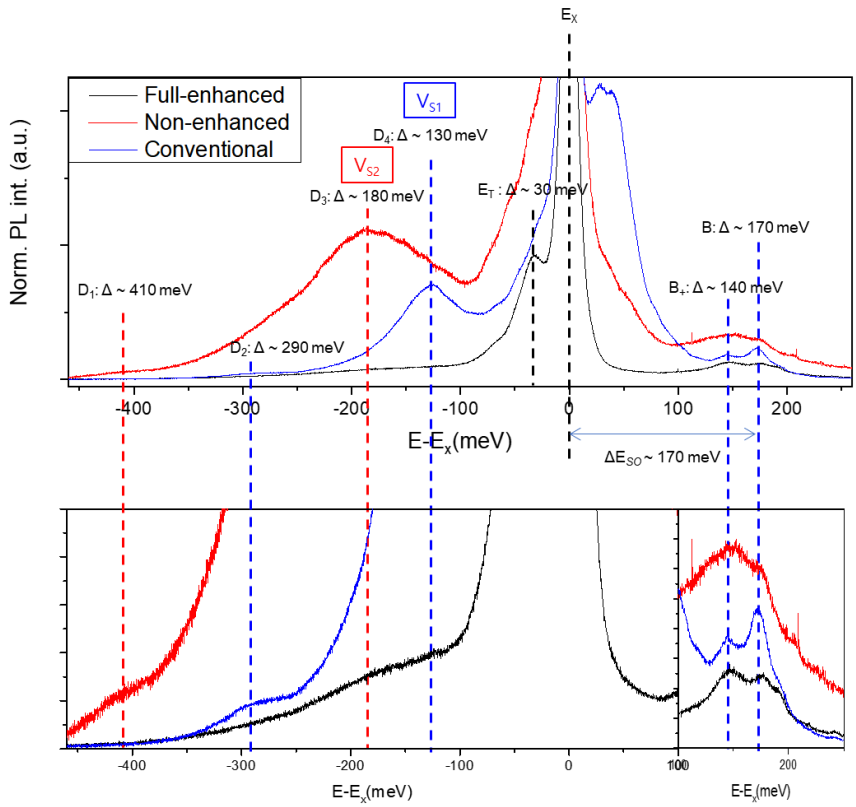

Figure 2.3 Low-temperature PL of MoS_2, as a function of growth method and before and after light illumination. Promoted-grown MoS_2 after light illumination (black), promoted-grown MoS_2 before light illumination (red), and conventional CVD-grown MoS_2 (blue).

In order to investigate the effect of defect healing on the electronic properties of MoS_2, I performed X-ray photoelectron spectroscopy (XPS) measurements before and after the healing process. By comparing the XPS spectra, I was able to analyze the changes in the Fermi level and gain insights into the healing mechanism of defects in MoS_2.

To accurately assess the changes in the XPS spectra, I calibrated the spectra using a C calibration. By aligning the carbon peak, I ensured that any observed shifts in the spectra were not due to instrumental factors but rather inherent changes in the MoS_2 material.

Upon examining the XPS spectra before and after defect healing, I observed an intriguing behavior. The peak corresponding to oxygen, which is not directly involved in defect-related processes, remained unchanged in both spectra. However, significant redshifts were observed in the XPS spectra of both Mo and S elements.

The redshift observed in the Mo XPS spectrum indicates a downward shift of the binding energy (Figure 2.4a). suggesting a decrease in the Fermi level. This shift is consistent with the healing of defects, particularly sulfur vacancies, which are known to introduce mid-gap states in MoS_2. The disappearance of these mid-gap states due to defect healing leads to a reduction in electron trap states,

thereby lowering the Fermi level.

Similarly, the redshift observed in the S XPS spectrum further supports the healing of sulfur vacancies. The decrease in binding energy for sulfur indicates a change in its electronic state (Figure 2.4b). which is associated with the elimination of sulfur vacancies and the reduction of mid-gap states. [83, 84]

The observed redshifts in both Mo and S XPS spectra provide strong evidence for the healing of defects in MoS_2 through our defect healing process.

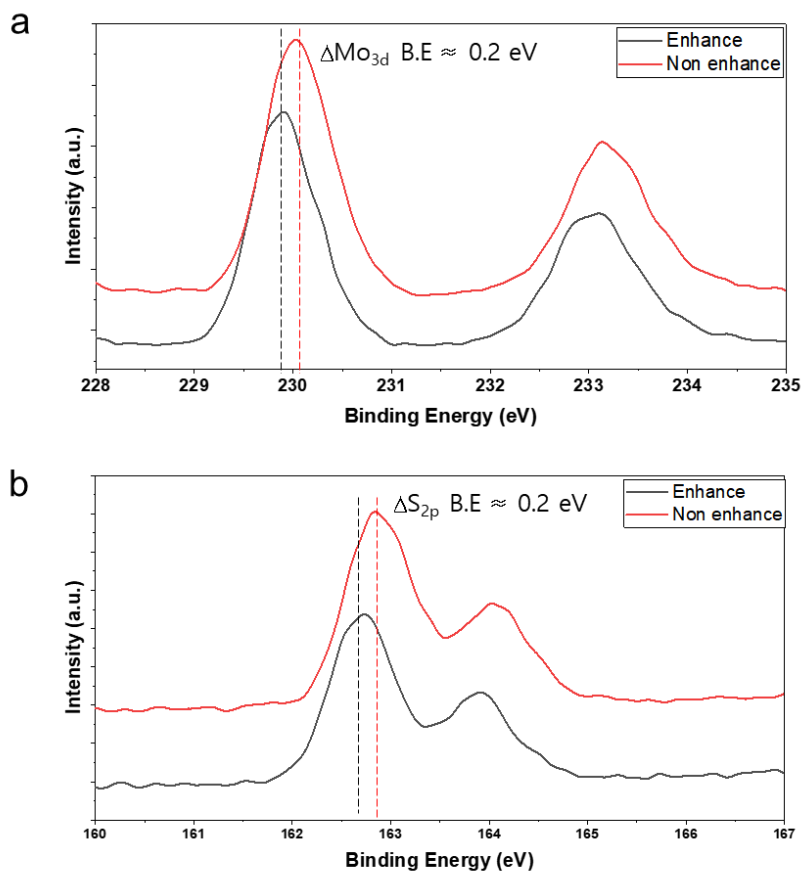

Figure 2.4 XPS measurement results before and after illumination. The binding energy of (a) Mo and (b) S

2.1.4. Conclusion

In conclusion, I successfully modified a microscope setup to investigate the PL of MoS_2. Through PL imaging, I observed a gradual enhancement in PL intensity within the imaging area, resulting from repetitive light illumination. The point PL measurements provided quantitative evidence of approximately 7-fold enhancement in PL intensity. And low-temperature PL measurements on the synthesized MoS_2 films revealed distinct PL characteristics among the samples with different growth conditions. The use of a promoter resulted in a significant reduction in defect-bound PL intensity after repeatable light illumination. The energy differences in the defect-bound exciton peaks further suggested different defect types, with di-sulfur vacancies being favored under Mo-rich growth conditions. These findings contribute to our understanding of the influence of growth conditions and promoters on the defect properties of MoS_2. These findings contribute to our understanding of the behavior of MoS_2 under light exposure and provide insights for developing strategies to enhance the PL properties of MoS_2 for various optoelectronic applications.

2.2. WO_x-driven growth of 2H- and 3R-WS_2 multilayers by physical vapor deposition

2.2.1. Introduction

Numerous studies have focused on the distinctive optical and electronic properties of monolayer TMDs. [85-89] However, multilayers with various stacking orders, such as trigonal, hexagonal, and rhombohedral, have shown intriguing atomic-scale optical properties with non-linearity, which is beneficial for various optical applications. Nevertheless, controlling the stacking order of TMD multilayers is still challenging because of low-yield expectations from mechanical exfoliation and difficulties in fabrication of artificial stacks with specific angles. [90-92] Despite efforts to control stacking order through artificial stacks, impurities and partial atomic reconstruction during the interlayer transfer process often lead to non-uniform properties in artificially formed multilayers, limiting industrial-scale applications. Although various growth methods for 2D materials have been developed to overcome this challenge, growth mechanisms remain unclear. Here, I report the growth of multilayer WS_2 single crystals with 2H- and 3R- stacking orders using liquid-phase tungsten oxide (WO_x)-driven growth. I find that the WO_x plays an important role

during growth of WS_2. The liquid phase WO_x with high concentration of tungsten efficiently nucleates and grows the multilayer WS_2 crystals with various layer numbers and stacking orders, facilitating the Vapor-Liquid-Solid (VLS) growth of WS_2. The few-layers (>1L) of WS_2 exhibits changes in indirect exciton and Raman shift due to differences in band characteristics and interlayer coupling depending on the stacking order, and even shows second harmonic signals depending on the presence of inversion symmetry breaking.

2.2.2. Experimental procedure

PVD process

WS_2 growth by physical vapor deposition: WS_2 on SiO_2 (285 nm)/si substrate was grown using the PVD system. Before the growth process, the substrates (2 × 6 cm^2) were cleaned via sonication in acetone and isopropyl alcohol for 10 min each. A tungsten disulfide powder (WS_2, 1.2 g, Alfa Aesar)-loaded alumina boat was heated to 1100 °C at the center of the furnace. The substrate was positioned 14 ~ 20 cm away from the center of the furnace. And the temperature of furnace was ramped up to the reaction temperature of 1100 °C with a ramping rate of 22 °C /min. The reaction was maintained for 1 hr by supplying Ar gas (500 sccm) for carrying W-contained species vapors to the substrate. After the growth, the furnace was cooled naturally to

300 ℃ followed by rapid cooling.

Scanning Transmission Electron Microscopy

A focused ion beam (FIB) system (Helios G4, Thermo Fisher Scientific, USA) was used for cross-sectional TEM. I used STEM (JEM-ARM200F (Cold FEG, JEOL Ltd., Japan)) at a low operating voltage of 80 keV.

Atomic force microscopy

AFM images were measured using NX-10 (Park Systems). Both contact and noncontact modes were performed considering the status of the samples and environment.

Second Harmonic Generation measurement

For the SHG measurements, I used a supercontinuum laser combined with a monochromator (LLTF CONTRAST-SR-EXTENDED-HP8) as the excitation source. A short-pass filter with a cutoff wavelength of 1,000 nm was used to block the laser beam from entering the spectrometer (Horiba TRIAX 320). The SHG signal was detected using a thermoelectrically cooled back-illuminated CCD detector. The laser power measured just before the objective was kept

at 3 mW. To measure the polarization dependence of the SHG, a superachromatic half-waveplate (Thorlabs SAHWP05M-700) was used to rotate the polarization of the linearly polarized laser beam to the desired direction. The analyzer angle was set such that only the photons with a polarization parallel to the incident polarization passed through. Another achromatic half-waveplate was placed in front of the spectrometer to keep the polarization direction of the signal entering the spectrometer constant with respect to the groove direction of the grating.

Raman Spectroscopy

The Raman intensity map image and spectra were acquired using Raman spectroscopy (LabRAM HR Evolution) with a 532 nm laser. To minimize the damage to the sample from laser irradiation, a power of < 5 mW was used for an acquisition time of 10 s. As the laser spot size was ≈1 μm, the mapping area was scanned at a point-to-point distance of 1 μm. All the measurements were conducted at room temperature after cooling the annealed samples.

2.2.3. Results and Discussion

I synthesized the multilayer WS_2 crystals on a SiO_2 substrate at 1000°C by physical vapor deposition as shown in Fig. 2.5a (see Methods for details). The WS_2 powder was placed in the middle of the furnace as a precursor for thermal decomposition. The SiO_2 substrate near the outlet zone has different temperature of 800-1000°C. Depending on the temperature of the substrate, the grown WS_2 crystals showed different morphologies (Fig. 2.5b).

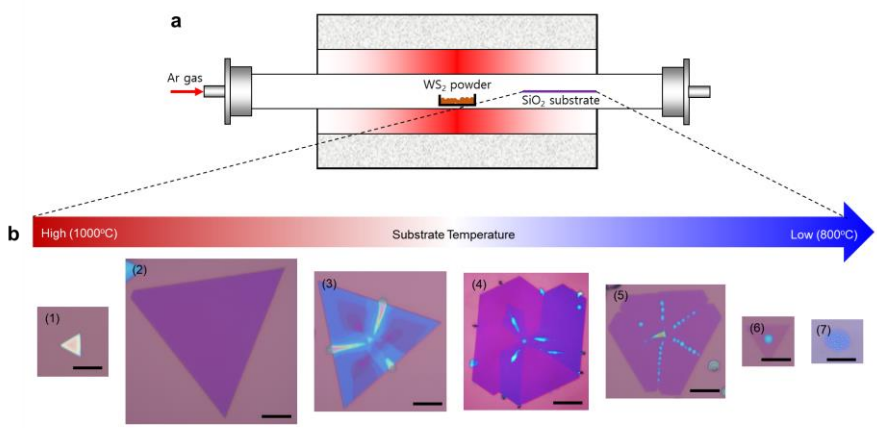

Figure 2.5 (a) Schematic illustration of PVD process for synthesis of the multilayer WS_2 crystals. (b) Optical microscopic images of the grown WS_2 crystals on different positions of the SiO_2 substrate at different temperatures. The scale bar is 10 μm.

Even though the uniform multilayers WS_2 crystals are observed on some location of the substrate, the synthesized WS_2 crystal in the middle of the substrate has different thicknesses and cyan particles as shown in Figure 2.6a. To investigate the crystal structure of WS_2 and particles, I measured Raman spectra from different positions of Fig. 2.6a (indicated by blue, green, pink, red, and black circles) as shown in Fig. 2.6b. The black Raman spectrum was obtained from the black particle at the edge of WS_2 grain. No vibration mode was observed here. Blue and pink Raman are 3L and 4L Raman spectra, respectively. In the Raman of 3L, the Raman shift difference between the E^1_{2g} and A_{1g} peaks is 68 cm^{-1}, and the 4L is 68.7 cm^{-1}, showing the difference depending on the layer thickness. [93] The red Raman spectrum was obtained from the cyan particle in WS_2 grain inner. No vibration mode was observed here except the Raman peak of WS_2. This indicates that the cyan particles are amorphous materials. The black Raman spectrum was obtained from the SiO_2 substrate for comparison. As a result, peaks with different crystals than the signature peak of WS_2 did not appear. For elemental analysis of the cyan particles, I obtained elemental line profile along the white dotted line of Fig. 2.6a using the energy dispersive spectroscopy (EDS) in scanning electron microscopy (SEM). The EDS profiles of Fig. 2.6c and d for tungsten

and oxygen show that the particle is highly concentrated region of tungsten and oxygen, indicating that the elongated particles in the WS_2 crystal is WO_x.

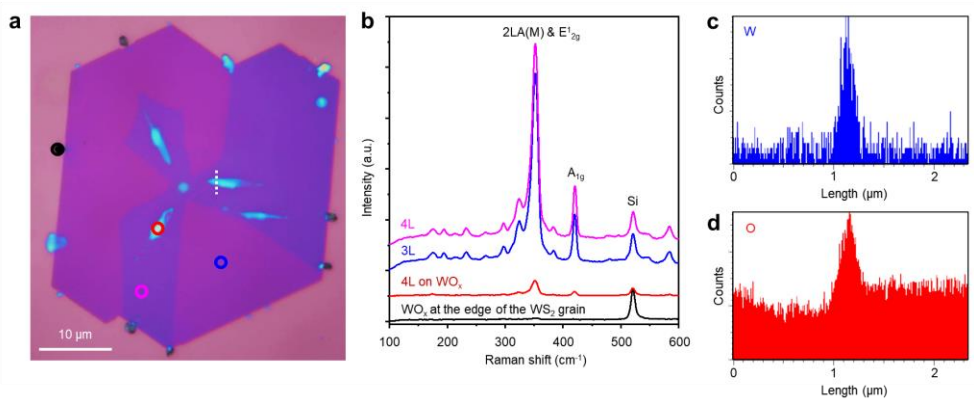

Figure 2.6 Structural and elemental analyses of the PVD-grown WS_2 crystals. (a) Optical microscopic image of the PVD-grown WS_2 crystal with different thicknesses and cyan particles. (b) Raman spectra of the PVD-grown WS_2. The Raman spectra of different colors corresponds to the colored circles in Fig. 2.6a. Elemental line profiles obtained from the white dotted line of Fig. 2.6a: (c) W and (d) O.

To conduct a thorough structural analysis of the WOx and WS_2/WO_x area, I utilized cross-sectional TEM and EDS mapping (Fig. 2.7). Figure 2.7a shows the cross-sectional TEM of the spherical particle obtained along the white dotted line in the inset of Fig. 2.7a, which is formed in the substrate region of (7). Figure 2.7a clearly shows that the SiO_2 is etched by the particle. The EDS maps of Fig. 2.7b show that W and O are uniformly detected without any signal of S, indicating that the spherical particles formed on the SiO_2 region of (7) are WO_x. Figure 2.7c shows the cross-section TEM of the ellipsed particle with WS_2 grain obtained along the white dotted line in the inset of Fig. 2.7c, which is formed in the substrate region of (3~4). In Figure 2.7c shows that the WO_x located under the WS_2 layer with SiO_2 etching. The EDS maps of Figure 2.7d show that W and O are uniformly detected in lower particle. And W and S signal detected in upper WS_2 layer. Indicating that WO_x is located under the WS_2 layer. Through XPS measurements of WO_x and WS_2/WO_x area, it shows that only tungsten oxide was formed in the region of (7), and in both types of samples, bonding between W and O was formed in oxygen bonding. (Figure 2.8a - h)

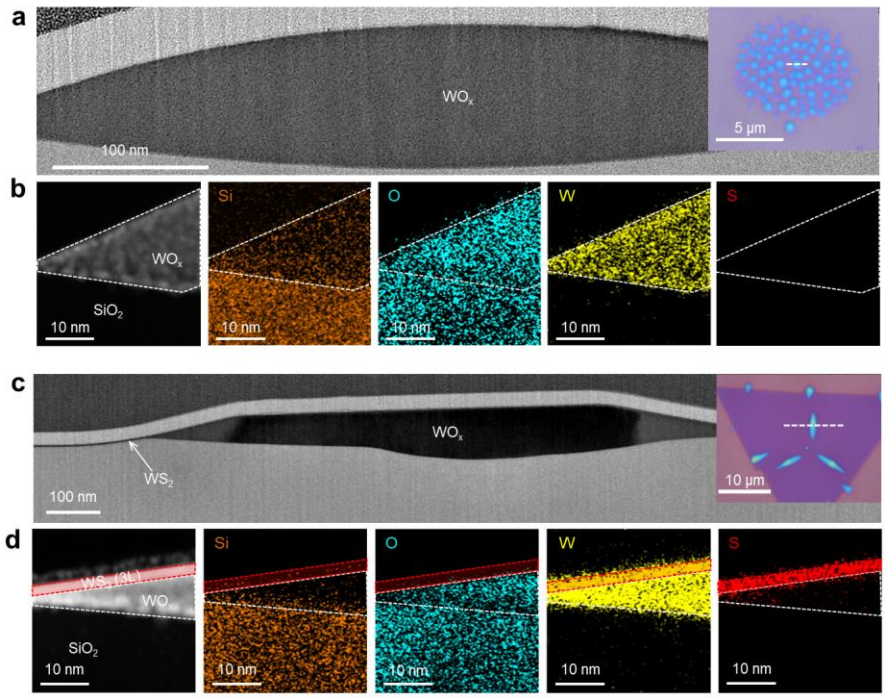

Figure 2.7 Structural analysis of the WO_x particle and WS_2/WO_x heterostructure. (a) Cross-sectional TEM image of the WO_x particle obtained from the white dotted line of the inset. The inset is optical microscopic image of the WO_x particles formed on the SiO_2 region (7). (b) EDS maps of Si, O, W, and S for the WO_x particle formed on the SiO_2 region (7). (c) Cross-sectional TEM image of the WS_2/WO_x heterostructure obtained from the white dotted line of the inset. The inset is optical microscopic image of the WS_2/WO_x heterostructure formed on the SiO_2 region (4). (b) EDS maps of Si, O, W, and S for the WS_2/WO_x heterostructure formed on the SiO_2 region (4).

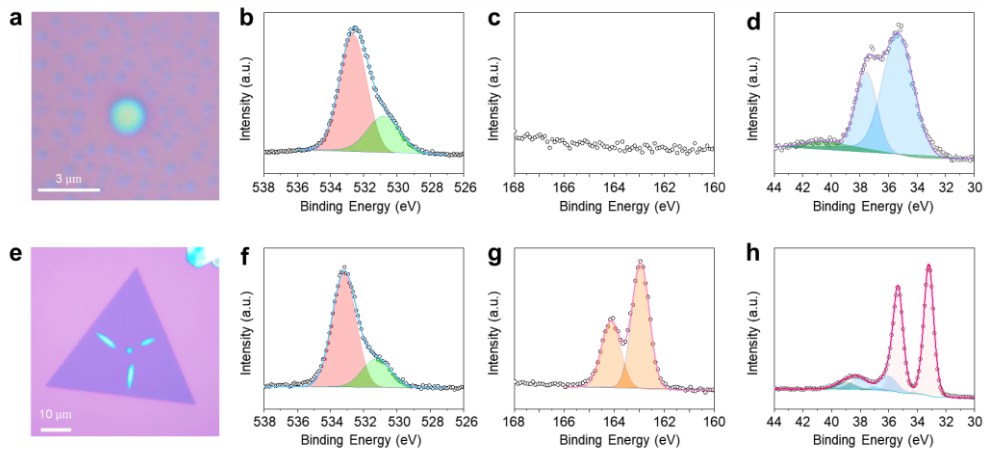

Figure 2.8 XPS measurement results for each region. (a) OM image and (b) binding energies of O, (c) S, and (d) W for the WO_x particle in region (7). (e) OM image and (f) binding energies of O, (g) S, and (h) W for the WS_2/WO_x heterostructure in region (4).

In Figure 2.9a, a tilted SEM analysis was performed to investigate the presence of tungsten oxide at the edges of the WS_2 particles. Tilted SEM images were captured to visualize the interface between WS_2 and tungsten oxide and to study their spatial relationship. The results show that the tungsten oxide is triply folded within the particles, which indirectly shows that the position of tungsten oxide is related to the growth direction of WS_2. As shown in the Figure 2.10, there are WO_x at the corners and edges of the grain, regardless of the shape of the grain in WS_2. The AFM height and lateral images (Figure 2.9b and c) provide a detailed view of the hexagonal shape of the WS_2 grain, offering valuable insights into its morphology. The images reveal distinct features that are crucial for understanding the growth and structural characteristics of the grain. In Figure 2.9b, it is intriguing to observe that the hexagonal-shaped grain exhibits a unique characteristic: one type of edge appears shorter and nearly straight, while the other edges display a slightly convex curvature. This difference in edge morphology is attributed to variations in the growth rates along different zigzag edges [94]. The contrasting growth rates contribute to the distinct edge shapes observed in the hexagonal WS_2 grain. Despite the variations in edge morphology, the formed WS_2 grain, as demonstrated in Figure 2.9c, exhibits a single lateral image

with a consistent phase throughout its structure. This suggests that the grain has grown conformally, maintaining a uniform phase across its surface. This observation aligns with the conformal growth characteristics typically associated with WS_2 growth processes.

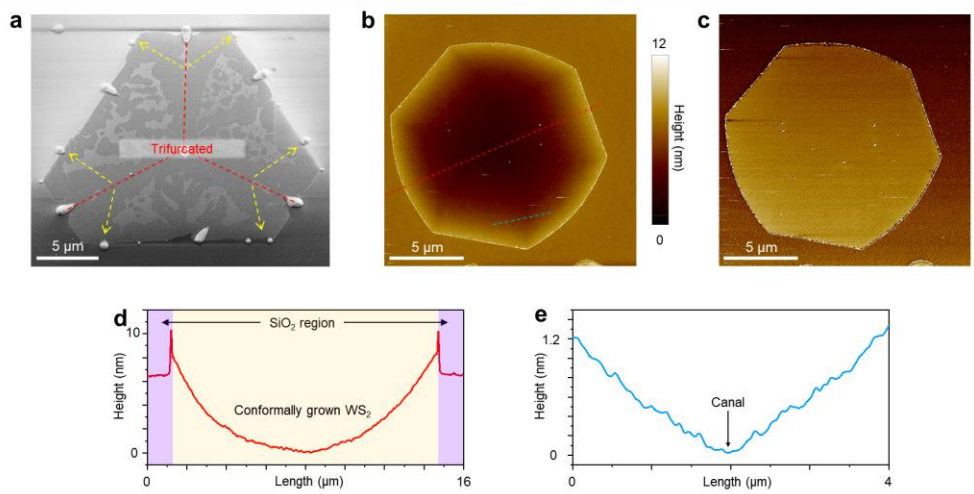

Figure 2.9 Structural analysis of grown WS_2 with tungsten oxide. (a) tilted SEM image of WS_2 grain with tungsten oxide at edge of the grain. (b) AFM height image and (c) lateral image of hexagonal shape WS_2. (d) height line profile of SiO_2-WS_2-SiO_2 (red dot line in b) and (e) height line profile of WS_2 with canal. (sky blue dot line in b)

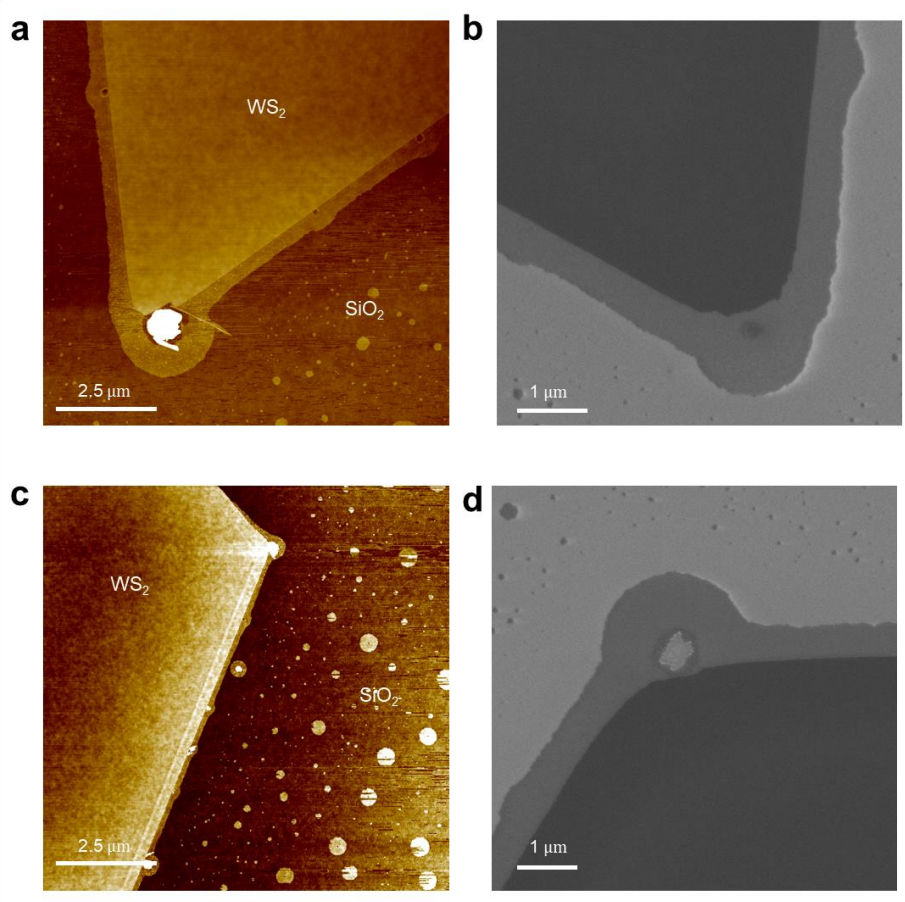

Figure 2.10 Verification of WO_x in grain corners by AFM and SEM measurements. (a) AFM image, (b) SEM image of a triangular-shaped grain corner. (c) AFM image, (d) SEM image of a hexagonal-shaped grain corner.

Bilayer WS_2 single crystals exhibit two distinct shapes: triangular and hexagonal. These shapes were observed in the grown WS_2 samples, indicating the presence of different crystal structures in the bilayer configuration (Figure 2.11a and b). The height profiles of the triangular and hexagonal shapes were determined using atomic force microscopy (AFM). For the triangular shape, the height was measured to be 1.96 nm relative to the SiO_2 substrate (Figure 2.11c). In contrast, the hexagonal shape exhibited a height of 1.94 nm (Figure 2.11d).

To investigate the stacking order of the two types of bilayer WS_2 grains, SHG measurements were performed. The SHG signals provide valuable information about the crystal symmetry and stacking arrangement. The results revealed that the triangular-shaped grains exhibited a strong SHG signal, indicating the breaking of inversion symmetry. This observation suggests the presence of the 3R stacking order in triangular-shaped bilayer WS_2. In contrast, the hexagonal-shaped grains did not show an SHG signal, indicating the dominance of the 2H stacking order in hexagonal-shaped bilayer WS_2 grains with inversion symmetry. (Figure 2.11e) In order to further characterize the optical properties of bilayer WS_2 structures, PL and Raman spectroscopy were conducted on the samples with confirmed stacking orders obtained from the SHG measurements. The PL spectrum of the

bilayer WS_2 structures revealed distinct features associated with band transitions. A prominent direct band transition corresponding to the A-exciton was observed at 1.94 eV. Additionally, an indirect band transition was observed near 1.72 eV. It is worth noting that the bilayers with different stacking orders exhibited variations in the valence band splitting, [95] leading to an approximately 20 meV difference in the energy of the indirect band transition (Figure 2.11f). Raman spectroscopy was employed to analyze the vibrational modes and interlayer coupling in the bilayer WS_2 structures. In Figure 2.11g, The Raman spectra revealed the presence of two characteristic fingerprinting peaks, namely A_{1g} and E^1_{2g}. The E mode originates from the in-plane vibration and typically exhibits a slight shift to lower frequency with increasing interlayer coupling. This behavior can be attributed to long-range Coulombic interlayer interactions and the associated dielectric screening effect. In contrast, the A' mode arises from the out-of-plane vibration and is slightly blue-shifted. This is due to interlayer coupling, which increases as the van der Waals restoring force strengthens. [96]

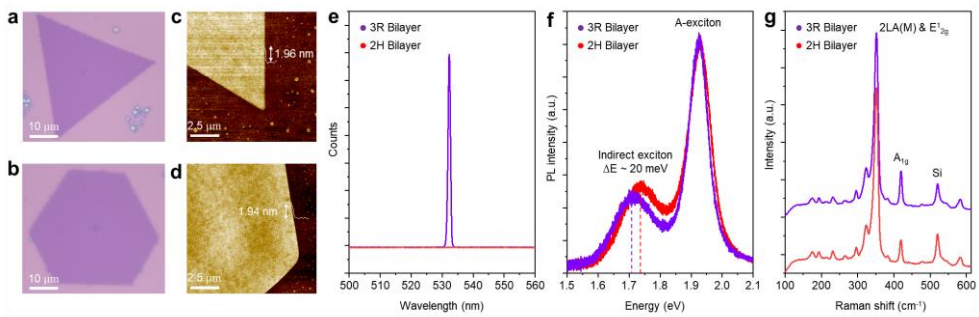

Figure 2.11 Optical properties and AFM measurement of grown two-types of WS_2 with different shape. (a) Optical microscope image of 3R bilayer WS_2. And (b) its AFM height image. (c) Optical microscope image of 2H bilayer WS_2. And (d) its AFM height image. (e) SHG spectrum of 2H and 3R bilayer WS_2. (f) Photoluminescence spectrum of 2H and 3R bilayer WS_2. (g) Raman spectrum of 2H and 3R bilayer WS_2.

I propose a growth mechanism for WS_2 grown by PVD based on the combined results. The WO_x liquid intermediate is formed through the embedding process of tungsten and oxygen, as shown in Figure 2.12a. During the physical vapor deposition (PVD) of WS_2, even at high temperatures, oxygen cannot be supplied for the decomposition of WS_2. However, the formation of WO_x during the synthesis process is attributed to the reaction between the decomposed species of WS_2 and oxygen from the SiO_2 substrate, as shown in Figure 2.12b and Figure 2.13. [97, 98] The formed WO_x liquid allows for the dissolution of sulfur, and the dissolved S exhibits a significantly long diffusion length within the liquid medium. It acts as a mediator for WS_2 nucleation at the surface of the liquid, as shown in Figure 2.12c. As a result of WS_2 nucleation, multiple layers of WS_2 grains are formed on the surface of the WO_x liquid. Subsequently, the additional dissolved S leads to the further growth of WS_2 grains at the edges of the WS_2 nuclei (Figure 2.12d). This growth mechanism differs from the previously reported self-limited monolayer growth reactions. [99, 100] In this case, the liquid surface acts as a mediator, eliminating the blocking effect caused by the increased dissolution and extended diffusion length of S within the liquid medium. [101] Unlike conventional self-limited reactions, where the reconfiguration of

surface metal atoms in the medium occurs and the transition metal dichalcogenide (TMD) is converted, the supply of chalcogen is hindered, making it difficult for additional layer growth to occur [99]. The WO_x liquid present between the WS_2 layers is squeezed out towards the outer side of the WS_2 grains due to the difference in surface energy. [102, 103] (Figure 2.12e) The final growth morphology depends on the relationship between the grain growth rate and the diffusion velocity of the WO_x liquid droplet. If the diffusivity of the WO_x liquid droplet is faster than the grain growth rate of WS_2, the WO_x continuously grows on the surface of the WS_2 grain, supplying the W source and extending the WS_2 grain. Ultimately, it solidifies at the edge of the grain, exposing itself as a WO_x droplet in the interface of the grown WS_2 grain. (Figure 2.12f and 2.12g) If the diffusivity of the WO_x liquid droplet is slower than the grain growth rate of WS_2, the WS_2 growth is terminated when it fully covers the surface of the WO_x droplet, leading to the solidification of the WO_x within. As a result, the remaining WO_x takes on an elongated elliptical shape following the slower growth direction of the WS_2 grain. This shape is due to the blocked supply of S within the WO_x droplet. (Figure 2.12h and i)

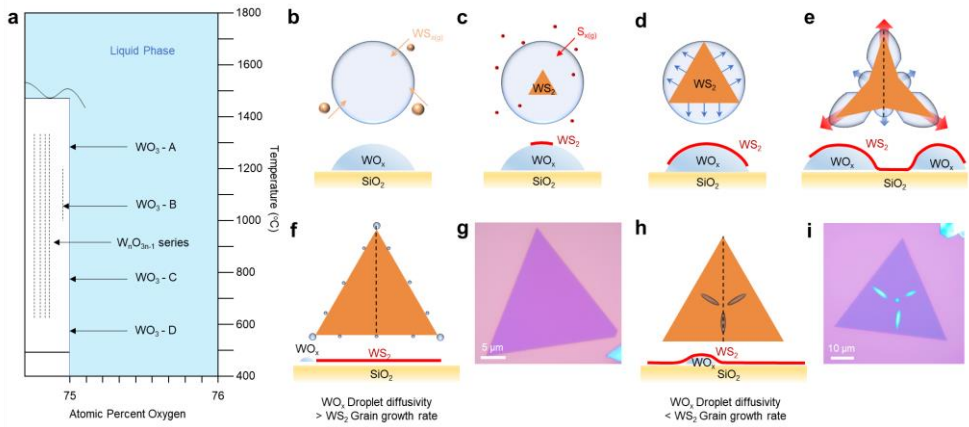

Figure 2.12 Phase diagram and Schematic illustration of the WS_2 growth assisted by liquid tungsten oxide. (a) Phase diagram of tungsten – oxygen system. The proposed mechanism of WO_x assisted growth of WS_2: (b) liquid droplet formation due to the reactions of vapor-phase tungsten species with oxygen in SiO_2 substrate by decomposition of WS_2 powder at high temperature. (c) Nucleation of WS_2 by dissolve S species by decompose of WS_2 powder. (d) Lateral growth of WS_2 continuous S dissolving. (e) Squeeze out of liquid Tungsten oxide droplet by driving force according to different surface energy. (f) If liquid droplet diffusivity was faster than WS_2 grain growth, tungsten oxide droplet fully driven and solidified out of the WS_2 grain edge. And (g) its optical image. (h) If liquid droplet diffusivity was slower than WS_2 grain growth, tungsten oxide droplet was confined at inner of the WS_2 grain. And (i) its optical microscope image.

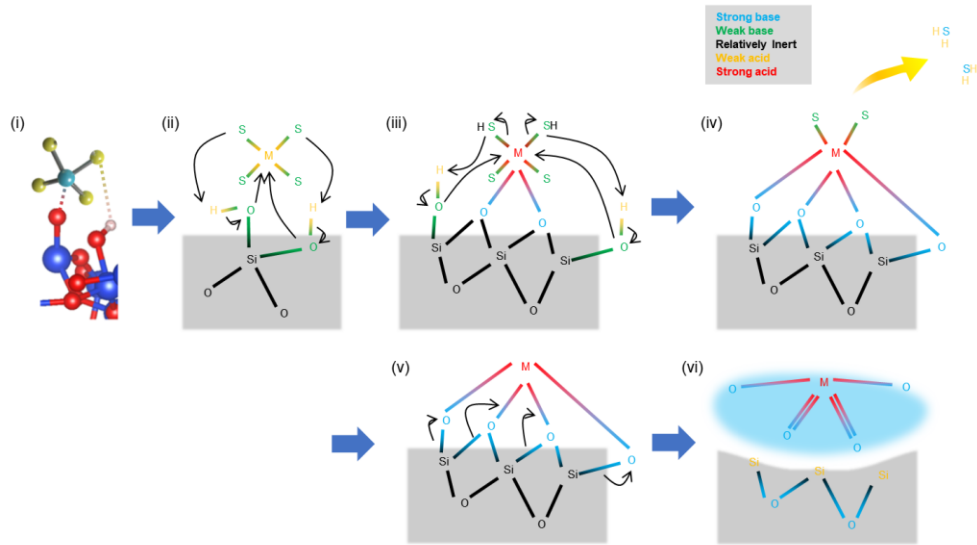

Figure 2.13 Proposed formation mechanisms of WO_x liquid intermediates. (i) The vaporized WS_{4-x} is adsorbed onto the SiO_2 substrate. (ii) It reacts with -OH groups on the SiO_2 surface to form the intermediate state of WO_xS_y. (iii-iv) Further reactions consume S. (v-vi) After S is consumed, M-O is formed. (v-vi) After all the S is consumed, the bond with Si is broken by the strong M-O bonding.

2.2.4. Conclusion

In this study, I synthesized few-layer single crystal WS2 on the SiO_2 substrate using PVD process and proposed growth mechanism of WO_x liquid intermediate. I demonstrated the growth of single crystal WS_2 with various layer numbers and stacking orders by forming a molten tungsten oxide with high oxygen ratio (more than 3) mediated by oxygen in SiO_2 substrate and utilizing it as an intermediate in the growth process. The W-O liquid not only serves as a precursor that supplies W for WS_2 growth but also provides a driving force for the continuous lateral growth of single crystal WS_2 grain based on the difference in surface energy. By controlling the degree of dissolution of sulfur, I have not only formed various layers of WS_2 (>1L) but also grown controlled various types of stacking order (2H or 3R) of single-crystal WS_2. Furthermore, the grown various types of WS_2 exhibits different second harmonic generation and photoluminescence properties depending on the layer number and stacking order because of band structure changes due to different interlayer couplings. Our results provide insight into the potential of non-linear optics in 2D materials using various layer numbers and stacking orders, as well as the growth of large-scale single crystal TMDs using metal oxide

intermediate assistance.

2.3. High quality monolayer MoS_2 film growth by sulfurization of faceted MoO_2

2.3.1. Introduction

Promising properties of 2D semiconductor materials have previously been reported. [104-110] Most studies on 2D materials still use 2D material flakes obtained by mechanical exfoliation. Various synthetic methods have been developed to improve the yield and scale of 2D materials, including Pulsed Layer Deposition (PLD), [111-113] Atomic Layer Deposition (ALD), [114-116] Chemical Vapor Deposition (CVD), [117] Metal-Organic Chemical Vapor Deposition (MOCVD), [118, 119] and sulfurization of Mo film [120, 121] or molybdenum oxide [122, 123] to synthesize MoS_2. However, several challenges are faced regarding the understanding of kinetics of the growth process and control of the quality and growth at the desired location. Among these methods, sulfurization has attracted attention for producing large-scale MoS_2 through the substitution of large-area films and homogeneous films. However, MoS_2 formed by sulfurization of various Mo-source-based materials (such as Mo metal film [120, 121] and MoO_3 [122, 123]) has been crystallized in a polycrystalline form with numerous randomly oriented domains and domain boundaries. Therefore, the quality of the film thereby formed shows relatively poor properties compared with

single-crystal two-dimensional materials synthesized differently. Here, I succeeded in synthesizing single-crystal MoS_2 by pre-growing metallic monoclinic MoO_2 crystals, followed by sulfurization. It was confirmed that the MoS_2 crystallized on the top surface of MoO_2 was crystallized epitaxially and aligned with a specific crystal direction of MoO_2. Although several layers of MoS_2 grow randomly by multi-nucleation near the edge of MoO_2, the top MoS_2 layer epitaxially crystallized on MoO_2 grows outward on SiO_2 to produce a high-quality single-layer MoS_2 grain and continuous film.

2.3.2. Experimental procedure

Monoclinic MoO_2 growth

MoO_2 on SiO_2 (285 nm)/Si substrate was grown using the atmospheric pressure CVD (APCVD) system. Before the growth process, the substrates (2×2 cm^2) were cleaned via sonication in acetone and isopropyl alcohol for 10 min each. A molybdenum trioxide powder (MoO_3, 5 mg, Sigma-Aldrich)-loaded alumina boat was heated to 750 ℃ at the center of the furnace. The substrate was positioned upside down on the MoO_3 powder-filled alumina boat, and the temperature of furnace was ramped up to the reaction temperature of 750 ℃ with a ramping rate of 50 ℃/min. The reaction was

maintained for 15 min by supplying Ar gas (300 sccm) for carrying MoO_{3-x} vapors to the substrate. After the growth, the furnace was cooled naturally to 600 ℃ followed by rapid cooling.

Sulfurization of Pre-grown MoO_2

The substrate on which MoO_2 was pre-grown was placed at the center of the furnace. Alumina boat filled with sulfur powder (S, 180 mg, Sigma-Aldrich) was placed 24 cm away from the furnace center toward the upstream (temperature of sulfur was measured as 180 ℃). Monolayer MoS_2 on a SiO_2 (285 nm)/Si substrate was synthesized using the APCVD system. The temperature of furnace was ramped up to the reaction temperature of 750 ℃ at a rate of 50 ℃/min. The reaction was maintained for 15 min by supplying Ar gas (300 sccm) to carry the sulfur vapor to the substrate. After the growth, the furnace was cooled naturally to 300 ℃ followed by rapid cooling.

Raman Spectroscopy

Raman and PL spectra were acquired using a Raman spectroscope with a 532 nm laser (Renishaw Raman, InVia Reflex Confocal Raman Microscope).

Scanning Transmission Electron Microscopy

A focused ion beam (FIB) system (Helios G4, Thermo Fisher Scientific, USA) was used for cross-sectional TEM. I used STEM (JEM-ARM200F (Cold FEG, JEOL Ltd., Japan)) at a low operating voltage of 80 keV.

Device Fabrication

To fabricate two-terminal MoO_2 devices, the regions for electrical contacts were patterned on a poly(methyl methacrylate) (PMMA) layer using e-beam lithography (Raith, Pioneer 2). Ti/Au (10 nm/40 nm) metal was deposited using an e-beam evaporator (KVE-E2000L, Korea Vacuum Tech). The samples were removed by soaking in acetone for 2 h at room temperature. Two-terminal MoS_2 devices were fabricated using the shaped MoS_2. To shape the MoS_2, PMMA layer was patterned via e-beam lithography, and XeF_2 gas was exposed to an open window using an XeF_2 etcher (SAMCO, VPE-4F). I exposed MoS_2 to XeF_2 gas for 12 min under an XeF_2 pressure of 3 Torr for complete etching. The electrode patterning and metallization process of the MoS_2 devices were the same as those used for the fabrication of MoO_2 devices.

Electrical Measurement

The electrical measurements of the MoO_2 and MoS_2 two-terminal devices were conducted using a semiconductor parameter analyzer (Keithley, 4200A-SCS 2400) under ambient conditions.

2.3.3. Results and Discussion

I first synthesized monoclinic MoO_2 crystals on a SiO_2 substrate using CVD, followed by sulfurization of the MoO_2 crystals, as shown in the schematic procedure and optical images in Figure 2.14 (see Experimental Procedures for details). To synthesize the MoO_2 crystals, MoO_3 powder was placed in the furnace in an alumina boat. Subsequently, a SiO_2 substrate was placed upside down on the boat, and the sublimation of MoO_3 powder was induced by ramping the furnace to 750 °C. MoO_{3-x} vapor species generated by MoO_3 sublimation led to MoO_2 nucleation and growth on SiO_2 substrates. As shown in the optical image in Figure 2.14a, rhombus-shaped MoO_2 crystals, tens of micrometers in size, were synthesized with sharp edges and a clean top surface. The Raman spectrum in Figure 2.14b shows that only MoO_2 crystals grow without formation of other phases such as MoO_3.[124] For sulfurization of the MoO_2 crystals, sulfur was supplied at 750 °C using sulfur powder in a

flow of Ar gas. The sulfur powder in the alumina boat was placed away from the furnace heating zone. As shown in the optical image of Figure 2.14c, MoS_2 was grown on the MoO_2 surface and stretched outward from MoO_2, whereas no dramatic change in the shape and size of the MoO_2 crystal was observed. The Raman spectra of the synthesized heterostructure in Figure 2.14d show that MoS_2 grew without collapse of the structure or crystallinity of MoO_2.

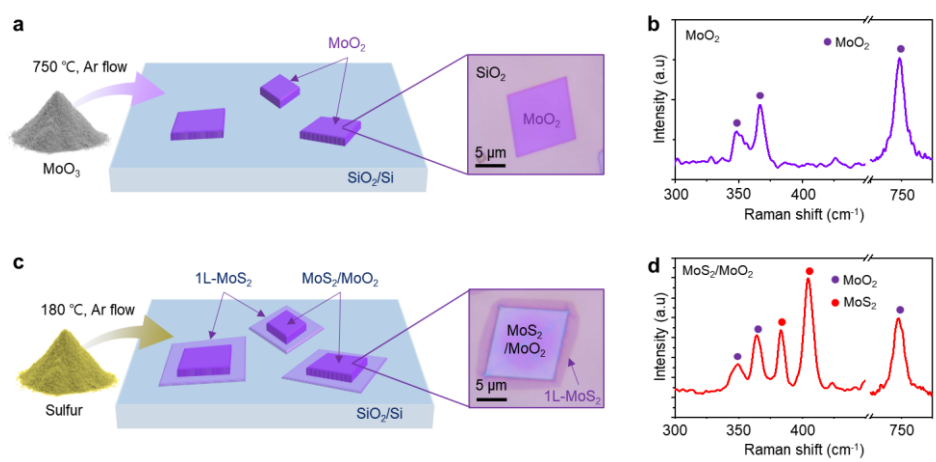

Figure 2.14 Growth of monoclinic MoO_2 crystals and sulfurization of MoO_2 into MoS_2/MoO_2 heterostructure. (a) Schematic illustration of MoO_2 crystal growth and optical microscopic image of the faceted MoO_2 crystal, (b) Raman spectrum of the MoO_2 crystal, (c) Schematic illustration of sulfurization of MoO_2 and optical microscopic image of the MoS_2/MoO_2 heterostructure. The 1L MoS_2 is grown on the SiO_2 substrate around edge of MoS_2/MoO_2 heterostructure, (d) Raman spectrum of the MoS_2/MoO_2 heterostructure.

Atomic force microscopy (AFM) was used to characterize the grown MoS_2/MoO_2 heterostructures, as shown in Figure 2.15; Figures 2.15a, b, and c show the AFM images of the synthesized MoO_2 crystal, whereas Figures 2.15d, e, and f show the AFM images of the sulfurized MoS_2/MoO_2 heterostructure. Figure 2.15a shows that a rhombus-shaped MoO_2 crystal was synthesized with an uneven top surface. As shown in Figure 2.15b, the grown MoO_2 has a thickness of ~23 nm. As shown in Figure 2.15c (obtained from the red area in Figure 2.15a), the top surface of MoO_2 has multiple steps and terraces owing to its nonlayered structure. After sulfurization of MoO_2, MoS_2 covers the entire MoO_2 crystal and stretches out to the SiO_2 region, as shown in Figure 2.15d and e. Meanwhile, the MoO_2 crystal maintains its shape after sulfurization. Although the MoO_2 crystal was fully covered by MoS_2, multiple steps and terraces were observed on the MoO_2 top surface in Figure 2.15f.

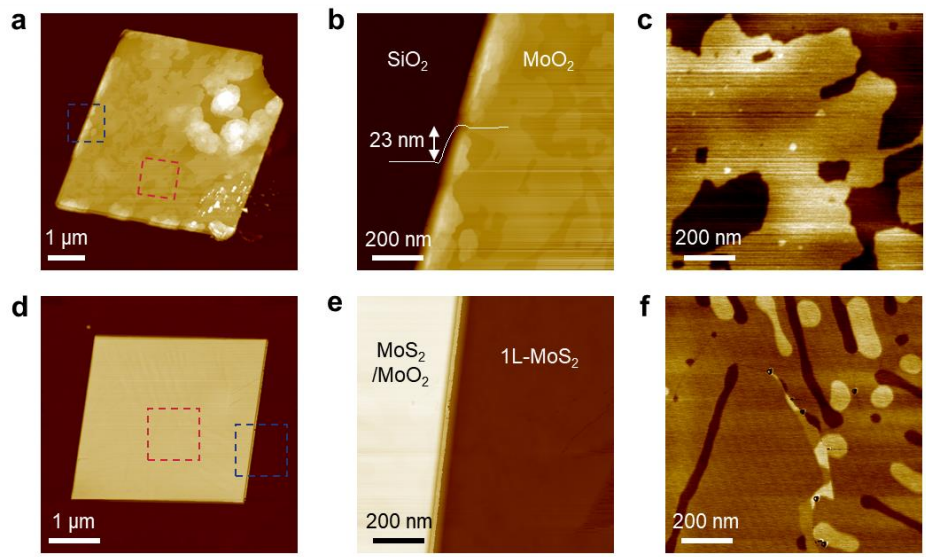

Figure 2.15 Morphologies of synthesized MoO_2 and MoS_2/MoO_2 heterostructure. (a) AFM image of the MoO_2 crystal. The magnified AFM images of (b) blue-dashed and (c) red-dashed regions of (a). (d) AFM image of the MoS_2/MoO_2 heterostructure. The magnified AFM images of (e) blue-dashed and (f) red-dashed regions of (d).

The atomic structures of the synthesized MoO_2 and MoS_2/MoO_2 heterostructures were investigated using transmission electron microscopy (TEM). The high-resolution TEM image in Figure 2.16a and selected area electron diffraction (SAED) pattern in Figure 2.16b shows that the synthesized MoO_2 is a monoclinic single crystal with a top surface of [121]. The (202) and (111) planes grew with lattice spacings of 0.280 and 0.232 nm, respectively. [125] TEM images in Figure 2.16c and e show the center and edge regions of the MoS_2/MoO_2 heterostructure, respectively. The Moiré pattern in Figure 2.16c appeared because of the difference in the crystal structures of MoS_2 and MoO_2 grown on the MoO_2 surface. [126] The SAED pattern in Figure 2.16d indicates that the crystalline MoS_2 is aligned to the MoO_2 crystal. Figure 2.16e shows that the edge region of the heterostructure has a Moiré pattern with two MoS_2 layers. As shown in the SAED pattern in Figure 2.16f, the two MoS_2 layers have a twist angle of 15.4°. Meanwhile, a single MoS_2 layer was observed on the SiO_2 region away from the edge of the heterostructure, as shown in Figure 2.16g and h. This result indicates that twisted MoS_2 layers are grown on the edge of the MoO_2 crystal, whereas only the MoS_2 monolayer stretches out toward the SiO_2 region.

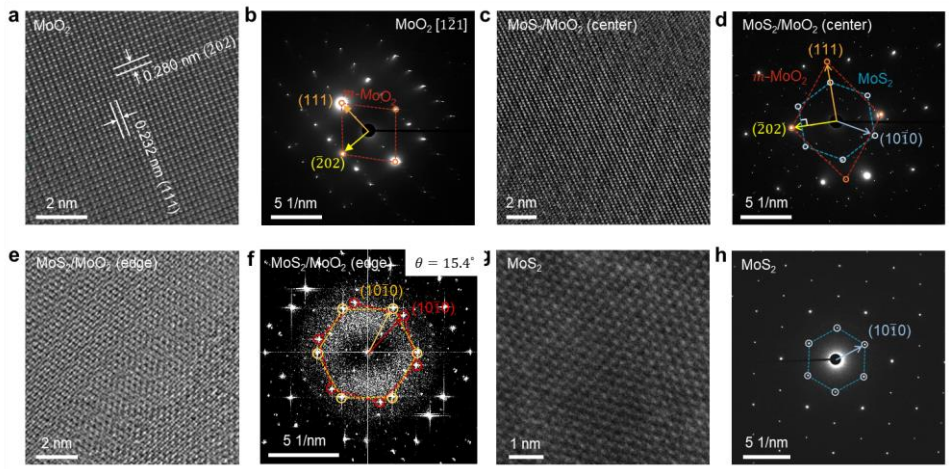

Figure 2.16 Atomic structures of the MoO_2 crystal, MoS_2/MoO_2 heterostructure, and 1L MoS_2. (a) TEM image (b) SAED pattern of monoclinic MoO_2 crystal. (c) TEM image and (d) SAED pattern of the center region of MoS_2/MoO_2 heterostructure. (e) STEM image and (f) FFT pattern of the edge region of MoS_2/MoO_2 heterostructure. (g) STEM image and (h) SAED pattern of 1L MoS_2 grown on SiO_2 around the edge of MoO_2.

To verify the nucleation sites and layered structure of MoS_2 on the MoO_2 crystal, the cross-section of the MoS_2/MoO_2 heterostructure was investigated using scanning transmission electron microscopy (STEM), as shown in Figure 2.17. In MoO_2, nucleation of MoS_2 occurs at the edge terrace and top surface sites of MoO_2. Therefore, MoS_2 grown from nucleation formed on different surfaces of MoO_2 grew while covering MoO_2. Figure 2.17a and b indicate that MoS_2 grown on the top surface covered the other MoS_2 grown on the edge. Thus, the top surface of MoO_2 is covered with only a single layer of MoS_2, and several layers of MoS_2 grow at the edge. Unusually, the MoS_2 layer initiated and grew from the top surface, extended to SiO_2, and grew (Figure 2.17c). This implies a different tendency than other MoS_2 growing in the existing layer-by-layer mode (LBL); in the conventional growth of multilayer MoS_2 by LBL growth, the layer at the bottom is the widest with a smaller grain size toward the top [127, 128] and ledge epitaxy by guidance of crystal direction of the substrate. [129] The result of the tilted MoS_2 grain in Figure 2.16e and cross-sectional image in Figure 2.17a confirm that MoS_2 grows independently at the top surface and edge of MoO_2 in the sulfurization of MoO_2; this is attributed to MoO_2 having different surface energies, depending on the Mo plane. [130] The twisted layers of MoS_2 grow at the

edge site of MoO_2 because of the nucleation of each layer at different steps.

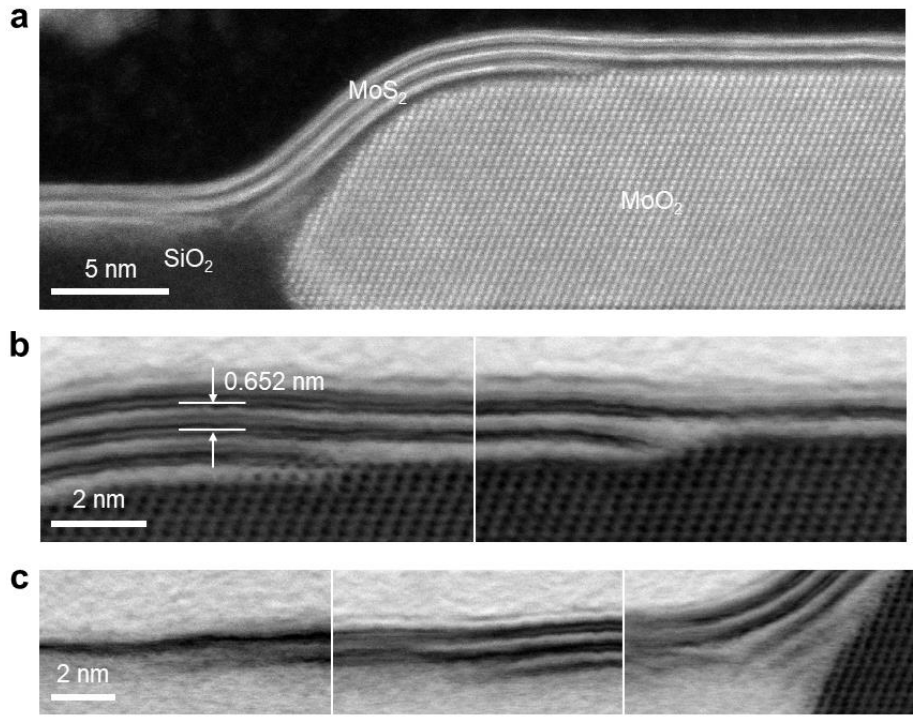

Figure 2.17 Growth of MoS_2 from the steps of MoO_2 crystal. (a) Cross-sectional STEM image of the MoS_2/MoO_2 heterostructure. (b) Combined two STEM images of the edge region of MoS_2/MoO_2 heterostructure. The MoS_2 layers nucleate from the steps of MoO_2. (c) Combined three STEM images of the MoS_2 extended onto the SiO_2 substrate. Note that only monolayer MoS_2 is grown on the SiO_2.

I performed optical measurements of the grown MoS_2 using Raman spectroscopy and photoluminescence (PL) measurements. Figure 2.18a shows an optical image of the measured MoS_2/MoO_2 heterostructure and extended grown monolayer MoS_2 on SiO_2. The two fingerprint Raman peaks of MoS_2, E^1_{2g} and A_{1g}, represent the in-plane and out-of-plane modes, respectively. [131] By plotting the two Raman peaks, E^1_{2g} and A_{1g}, the degree of strain and doping applied to MoS_2 can be confirmed. [132] In Figure 2.18b, the peaks of E^1_{2g} and A_{1g} are plotted by measuring the Raman spectra of the MoS_2 monolayer area on SiO_2 and MoO_2 in the sample shown in Figure 2.18a. The plot in Figure 2.18b shows that MoS_2 crystallized by sulfurization on MoO_2 (blue dots) exhibits a small compressive strain compared with MoS_2 grown on SiO_2 (red dots). The MoS_2 in the MoS_2/MoO_2 heterostructure is highly p-doped ($n = -1.5 \times 10^{12}$ to -2.0×10^{12}) compared with the MoS_2 on the SiO_2 substrate owing to the efficient charge transfer between MoS_2 and MoO_2. [133] I proceeded to measure the PL of MoS_2 to confirm that charge transfer occurs at the junction. The red spectra in Figure 2.18c are the PL spectra measured in the region corresponding to 1L MoS_2 in Figure 2.18a, and the blue spectra are the PL results measured in the MoS_2/MoO_2 heterostructure in Figure 2.18a. The PL of MoS_2 grown on SiO_2 is 5-fold stronger

than that of MoS_2 on MoO_2 because charge was transferred from MoS_2 to MoO_2 owing to the metallic characteristic (Figure 2.19) of MoO_2. Therefore, exciton recombination is reduced in case of MoS_2 on MoO_2, and the PL of MoS_2 on MoO_2 is quenched. [134]

As shown in the optical microscopic image in Figure 2.18d, the sulfurization of MoO_2 grown at an appropriate distance can produce a continuous film of outwardly grown monolayer MoS_2. I measured the optical properties of the continuous structure of MoS_2/MoO_2–MoS_2/SiO_2–MoS_2/MoO_2 through line Raman spectroscopy of the sample in Figure 2.18d. The existence of each material and trend of the MoS_2 Raman peak were confirmed through the waterfall plot in Figure 2.18d and contour plot image in Figure 2.20. To investigate the properties of grain boundary in the MoS_2 grown between two MoO_2 crystals, I obtained the waterfall plot of Raman spectra in Figure 2.18d and contour plot image of PL spectra in Figure 2.21. This result indicated that there is no recognizable difference at the grain boundary between two MoS_2 grains. [135, 136] As indicated by the out-of-plane and cross-sectional TEM and STEM results, MoS_2 grown on MoO_2 shows a relatively wide Raman shift difference compared with MoS_2 on SiO_2, despite the same monolayer. In the case of the MoS_2 monolayer grown on SiO_2, the Raman shift difference between

E^1_{2g} and A_{1g} is 20.6 cm^{-1} because the monolayer MoS_2 grown by CVD is affected by the substrate during the growth process, unlike mechanically exfoliated monolayer MoS_2. [137] In the MoS_2/MoO_2 heterostructure, a Raman-shift difference of ~23 cm^{-1} was observed because the A_{1g} peak of MoS_2 on MoO_2 is blue-shifted relative to that of MoS_2 on SiO_2. These results show that the Raman peak shift of MoS_2 is dominated by the effect of doping with MoO_2. [138]

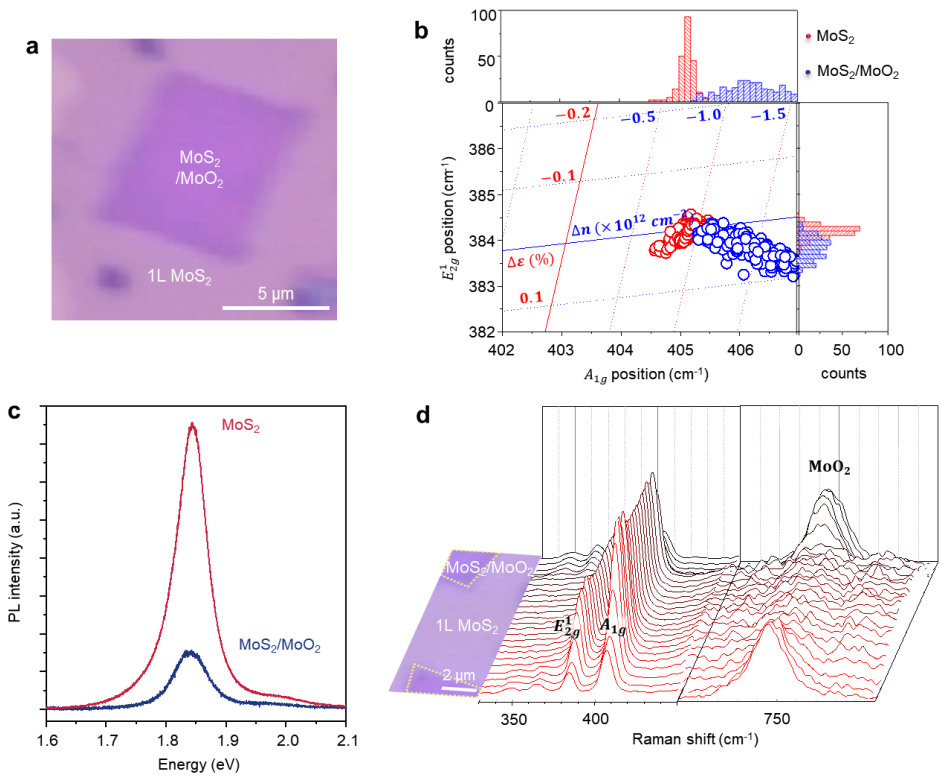

Figure 2.18 Optical properties of the MoS_2 and MoS_2/MoO_2 heterostructure. (a) Optical microscopic image of the MoS_2/MoO_2 heterostructure used for measurements of Raman and PL spectra. (b) Plot of Raman peak positions of the synthesized MoS_2 on the SiO_2 (red dots) and MoO_2 (blue dots). Strain and doping can be measured by using the red and blue axes, respectively. The red and blue distributions on the top and right panels indicate that the strain and doping levels are different for two MoS_2 regions on SiO_2 and MoO_2. (c) PL spectra of the 1L MoS_2 on the SiO_2 (red) and MoO_2 (blue). (d) Waterfall plots of Raman spectra measured from the MoS_2 grown

between two MoO_2 crystals. The Raman spectra were measured from the position as indicated in the optical image.

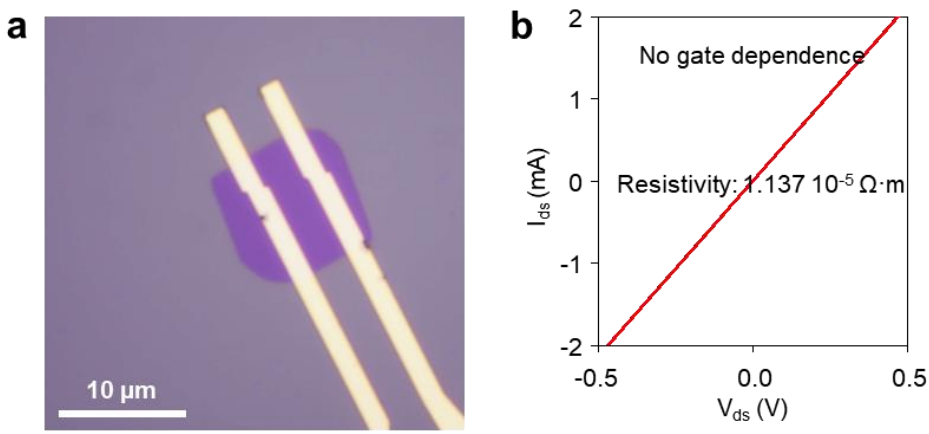

Figure 2.19 Electrical properties of monoclinic MoO_2. (a) Optical image of the MoO_2 grown on SiO_2/Si substrate. (b) Output curves (I_{DS}-V_{DS}) of the MoO_2 device

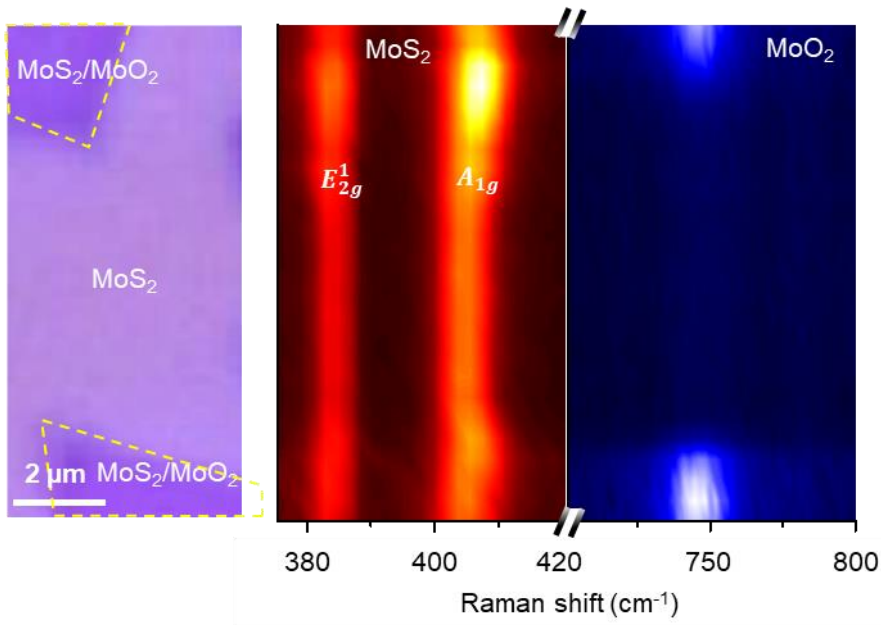

Figure 2.20 Contour plot of Raman spectra measured from the MoS_2 grown between two MoO_2 crystals. The Raman spectra were measured from the position as indicated in the optical image.

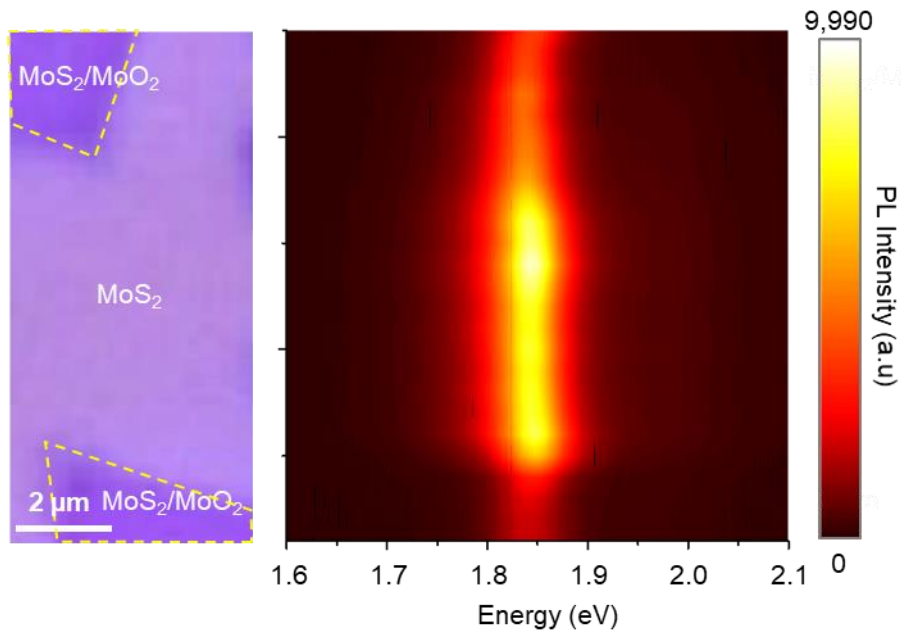

Figure 2.21 Contour plot of PL spectra measured from the MoS_2 grown between two MoO_2 crystals. The PL spectra were measured from the position as indicated in the optical image.

To characterize the electronic quality of the monolayer MoS_2 film grown on faceted MoO_2, I measured the transfer and output characteristics of the synthesized MoS_2 using SiO_2 as the back gate. Figure 2.22a shows an optical image of the patterned MoS_2 fabricated for the two-probe measurement. The output curve in Figure 2.22b shows that the synthesized MoS_2 transistor exhibited n-type characteristics and gate dependence. From the transfer curve in Figure 2.22c, the MoS_2 device has a mobility of 15.45 $cm^2 V^{-1} s^{-1}$ with an on/off ratio of $\sim 10^5$. This result suggests that the synthesized MoS_2 based on faceted MoO_2 has high quality and electrical properties.

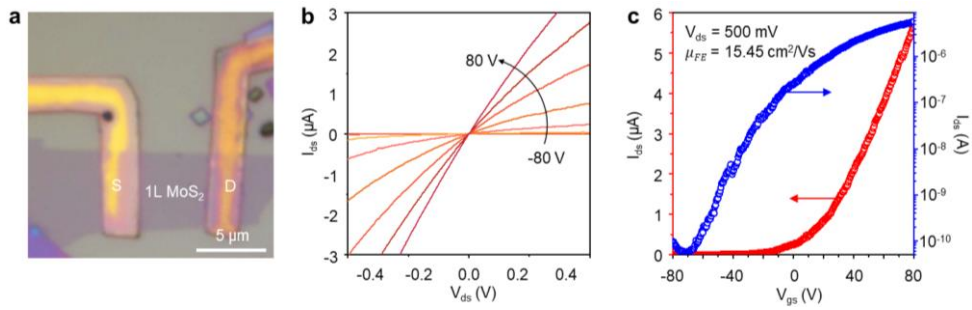

Figure 2.22 Electrical properties of the MoS_2 synthesized from MoO_2. (a) Optical microscopic image of the MoS_2 device. (b) Output curves (I_{DS}-V_{DS}) and (c) transfer curves (I_{DS}-V_{GS}) of the MoS_2 device.

2.3.4. Conclusion

In conclusion, I developed a growth method for high-quality MoS_2 using pre-grown faceted monoclinic MoO_2 as a growth template by improving the existing vapor-phase deposition method of the Mo-containing source. I succeeded in epitaxially growing MoS_2 by sulfurizing the [1$\bar{2}$1] plane of monoclinic MoO_2. The top MoS_2 layer epitaxially grown on MoO_2 was continuously grown on the SiO_2 substrate to form a monolayer of high-quality MoS_2, and the MoS_2 FET thus grown had a mobility of 15 $cm^2 V^{-1} s^{-1}$ and an on/off ratio of 10^5. This study not only demonstrates the growth potential of high-quality two-dimensional transition metal dichalcogenide materials and heterostructures by epitaxial growth of nonlayered and layered materials but also provides a methodology for crystal direction control and patterning of growing transition metal dichalcogenides (TMDs) by aligning MoO_2 crystals, in contrast to the sulfurization of amorphous Mo or MoO_x, which yields polycrystalline MoS_2.

Chapter 3. Summary

In this thesis, I introduced novel strategies for growth of desired transition metal dichalcogenides by modifying growth method. I have resolved many of the previously reported synthesis problems (high quality, scalability, growth rate, layer selectivity, stacking order control, etc.) by optimizing different growth methods and studying the growth mechanism. The novel growth strategies I studied are summarized in below.

- This study demonstrates the successful synthesis of large-scale MoS_2 using a NaBr promoter. The resulting films exhibit enhanced photoluminescence upon repeated light illumination. Low-temperature PL measurements and XPS analysis provide insights into the origin of the enhanced photoluminescence and confirm defect healing in the promoted-grown MoS_2 films. These findings contribute to advancing our understanding of the optical properties and defect engineering in large-scale MoS_2, paving the way for their utilization in various optoelectronic applications.

- Through physical vapor deposition of WS_2, I improved the problem of monolayer growth dominated by self-limited growth and synthesized WS_2 with several layers of different stacking orders.

During this process, I identified the growth mechanism driven by the WO_x liquid intermediate and found a way to overcome the self-limited growth.

- I report the nucleation and growth behaviors of monolayer MoS_2 by sulfurizing a faceted monoclinic MoO_2 crystal. The MoS_2 layers nucleated at the thickness steps of the MoO_2 crystal and grew epitaxially with crystalline correlation to the MoO_2 surface. The epitaxially grown MoS_2 layer expands outwardly on the SiO_2 substrate, resulting in a monolayer single-crystal film, despite multiple nucleation of MoS_2 layers on the MoO_2 surface owing to several thickness steps. High-quality monolayer MoS_2 film can be grown using the MoO_2 crystal as a seed and precursor. Our work demonstrates a route to grow high-quality MoS_2 using a faceted MoO_2 crystal and provides a deeper understanding of the nucleation and growth of 2D materials on a step-like surface.

As two-dimensional semiconductor transition metal chalcogenides are a key player in the scale-down of the next-generation semiconductor industry, I believe our strategy offers insight into the challenges currently facing mass production.

Reference

1. LIETH, R. M. A.; TERHELL, J. C. J. M., *Preparation and crystal growth of materials with layered structures*. Reidel Publishing Company, 1977.

2. Keum, D. H.; Cho, S.; Kim, J. H.; Choe, D.-H.; Sung, H.-J.; Kan, M.; Kang, H.; Hwang, J.-Y.; Kim, S. W.; Yang, H.; Chang, K. J.; Lee, Y. H., Bandgap opening in few-layered monoclinic $MoTe_2$. *Nat. Phy.* **2015,** *11* (6), 482-486.

3. Ali, M. N.; Xiong, J.; Flynn, S.; Tao, J.; Gibson, Q. D.; Schoop, L. M.; Liang, T.; Haldolaarachchige, N.; Hirschberger, M.; Ong, N. P.; Cava, R. J., Large, non-saturating magnetoresistance in WTe_2. *Nature* **2014,** *514* (7521), 205-8.

4. Chhowalla, M.; Shin, H. S.; Eda, G.; Li, L. J.; Loh, K. P.; Zhang, H., The chemistry of two-dimensional layered transition metal dichalcogenide nanosheets. *Nat. Chem.* **2013,** *5* (4), 263-75.

5. Song, I.; Park, C.; Choi, H. C., Synthesis and properties of molybdenum disulphide: from bulk to atomic layers. *RSC Adv.* **2015,** *5* (10), 7495-7514.

6. Manzeli, S.; Ovchinnikov, D.; Pasquier, D.; Yazyev, O. V.; Kis, A., 2D transition metal dichalcogenides. *Nat. Rev. Mater.* **2017,** *2* (8).

7. Kuc, A.; Heine, T., The electronic structure calculations of two-dimensional transition-metal dichalcogenides in the presence of external electric and magnetic fields. *Chem. Soc. Rev.* **2015,** *44* (9), 2603-14.

8. Splendiani, A.; Sun, L.; Zhang, Y.; Li, T.; Kim, J.; Chim, C. Y.; Galli, G.; Wang, F., Emerging photoluminescence in monolayer MoS_2. *Nano Lett.* **2010,** *10* (4), 1271-5.

9. Mak, K. F.; Lee, C.; Hone, J.; Shan, J.; Heinz, T. F., Atomically thin MoS_2: a new direct-gap semiconductor. *Phys. Rev. Lett.* **2010,** *105* (13), 136805.

10. Hill, H. M.; Rigosi, A. F.; Rim, K. T.; Flynn, G. W.; Heinz, T. F., Band Alignment in MoS_2/WS_2 Transition Metal Dichalcogenide Heterostructures Probed by Scanning Tunneling Microscopy and Spectroscopy. *Nano. Lett.* **2016,** *16* (8), 4831-7.

11. Zhu, Z. Y.; Cheng, Y. C.; Schwingenschlögl, U., Giant spin-orbit-induced spin splitting in two-dimensional transition-metal dichalcogenide semiconductors. *Phys. Rev. B* **2011,** *84* (15).

12. Kormányos, A.; Burkard, G.; Gmitra, M.; Fabian, J.; Zólyomi, V.; Drummond, N. D.; Fal'ko, V., k · p theory for two-dimensional transition metal dichalcogenide semiconductors. *2D Mater.* **2015,** *2* (2).
13. Xiao, D.; Liu, G. B.; Feng, W.; Xu, X.; Yao, W., Coupled spin and valley physics in monolayers of MoS_2 and other group-VI dichalcogenides. *Phys. Rev. Lett.* **2012,** *108* (19), 196802.
14. Pulkin, A.; Yazyev, O. V., Spin- and valley-polarized transport across line defects in monolayer MoS_2. *Phys. Rev. B* **2016,** *93* (4).
15. Habe, T.; Koshino, M., Spin-dependent refraction at the atomic step of transition-metal dichalcogenides. *Phys. Rev. B* **2015,** *91* (20).
16. Golberg, D., Nanomaterials: Exfoliating the inorganics. *Nat. Nanotechnol.* **2011,** *6* (4), 200-1.
17. Liu, F.; Wu, W.; Bai, Y.; Chae, S. H.; Li, Q.; Wang, J.; Hone, J.; Zhu, X.-Y., Disassembling 2D van der Waals crystals into macroscopic monolayers and reassembling into artificial lattices. *Science* **2020,** *367*, 903-906.
18. Desai, S. B.; Madhvapathy, S. R.; Amani, M.; Kiriya, D.; Hettick, M.; Tosun, M.; Zhou, Y.; Dubey, M.; Ager, J. W., 3rd; Chrzan, D.; Javey, A., Gold-Mediated Exfoliation of Ultralarge Optoelectronically-Perfect Monolayers. *Adv. Mater.* **2016,** *28* (21), 4053-8.
19. Moon, J.-Y.; Kim, M.; Kim, S.-I.; Xu, S.; Choi, J.-H.; Whang, D.; Watanabe, K.; Taniguchi, T.; Park, D. S.; Seo, J.; Cho, S. H.; Son, S.-K.; Lee, J.-H., Layer-engineered large-area exfoliation of graphene. *Sci. Adv.* **2020,** *6*, eabc6601.
20. Novoselov, K. S.; Geim, A. K.; Morozov, S. V.; Jiang, D.; Zhang, Y.; Dubonos, S. V.; Grigorieva, I. V.; Firsov, A. A., Electric Field Effect in Atomically Thin Carbon Films. *Science* **2004,** *306*, 666-669.
21. Novoselov, K. S.; Jiang, D.; Schedin, F.; Booth, T. J.; Khotkevich, V. V.; Morozov, S. V.; Geim, A. K., Two-dimensional atomic crystals. *Proc. Natl. Acad. Sci.* **2005,** *102* (30), 10451–10453.
22. Shen, Z.; Li, J.; Yi, M.; Zhang, X.; Ma, S., Preparation of graphene by jet cavitation. *Nanotechnology* **2011,** *22* (36), 365306.
23. Dular, M.; Stoffel, B.; Širok, B., Development of a cavitation erosion model. *Wear* **2006,** *261* (5-6), 642-655.
24. Lohse, D., Cavitation hots up. *Nature* **2005,** *434*, 33-34.
25. Hernandez, Y.; Nicolosi, V.; Lotya, M.; Blighe, F. M.; Sun, Z.; De, S.;

McGovern, I. T.; Holland, B.; Byrne, M.; Gun'Ko, Y. K.; Boland, J. J.; Niraj, P.; Duesberg, G.; Krishnamurthy, S.; Goodhue, R.; Hutchison, J.; Scardaci, V.; Ferrari, A. C.; Coleman, J. N., High-yield production of graphene by liquid-phase exfoliation of graphite. *Nat. Nanotechnol.* **2008,** *3* (9), 563-8.

26. Coleman, J. N.; Lotya, M.; O'Neill, A.; Bergin, S. D.; King, P. J.; Khan, U.; Young, K.; Gaucher, A.; De, S.; Smith, R. J.; Shvets, I. V.; Arora, S. K.; Stanton, G.; Kim, H.-Y.; Kangho Lee; Kim, G. T.; Duesberg, G. S.; Hallam, T.; Boland, J. J.; Wang, J. J.; Donegan, J. F.; Grunlan, J. C.; Moriarty, G.; Shmeliov, A.; Nicholls, R. J.; Perkins, J. M.; Grieveson, E. M.; Theuwissen, K.; McComb, D. W.; Nellist, P. D.; Nicolosi, V., Two-Dimensional Nanosheets Produced by Liquid Exfoliation of Layered Materials. *Science* **2011,** *331*, 568-571.

27. Whittingham, M. S.; Jr., F. R. G., THE LITHIUM INTERCALATES OF THE TRANSITION METAL DICHALCOGENIDES. *Mat. Res. Bull.* **1975,** *10*, 363-372.

28. Liyanage, A. U.; Lerner, M. M., Use of amine electride chemistry to prepare molybdenum disulfide intercalation compounds. *RSC Adv.* **2014,** *4* (87), 47121-47128.

29. PY, M. A.; HAERING, R. R., Structural destabilization induced by lithium intercalation in MoS_2 and related compounds. *Can. J. Phys.* **1983,** *61*, 76-84.

30. Benavente, E.; Ana, M. A. S.; Mendiza´bal, F.; Gonza´lez, G., Intercalation chemistry of molybdenum disulfide. *Coord. Chem. Rev.* **2002,** *224*, 87–109.

31. Huang, Y.; Wu, J.; Xu, X.; Ho, Y.; Ni, G.; Zou, Q.; Koon, G. K. W.; Zhao, W.; Castro Neto, A. H.; Eda, G.; Shen, C.; Özyilmaz, B., An innovative way of etching MoS_2: Characterization and mechanistic investigation. *Nano Res.* **2013,** *6* (3), 200-207.

32. Wu, J.; Li, H.; Yin, Z.; Li, H.; Liu, J.; Cao, X.; Zhang, Q.; Zhang, H., Layer thinning and etching of mechanically exfoliated MoS_2 nanosheets by thermal annealing in air. *Small* **2013,** *9* (19), 3314-9.

33. Yamamoto, M.; Einstein, T. L.; Fuhrer, M. S.; Cullen, W. G., Anisotropic Etching of Atomically Thin MoS_2. *J. Phys. Chem. C* **2013,** *117* (48), 25643-25649.

34. Lu, X.; Utama, M. I. B.; Zhang, J.; Zhao, Y.; Xiong, Q., Layer-by-layer thinning of MoS_2 by thermal annealing. *Nanoscale* **2013,** *5* (19), 8904-8908.

35. Castellanos-Gomez, A.; Barkelid, M.; Goossens, A. M.; Calado, V. E.; van der Zant, H. S.; Steele, G. A., Laser-thinning of MoS_2: on demand generation of a single-layer semiconductor. *Nano Lett* **2012,** *12* (6), 3187-92.

36. Liu, Y.; Nan, H.; Wu, X.; Pan, W.; Wang, W.; Bai, J.; Zhao, W.;

Sun, L.; Wang, X.; Ni, Z., Layer-by-Layer Thinning of MoS_2 by Plasma. *ACS Nano* **2013,** *7* (5), 4202–4209.

37. Brent, J. R.; Savjani, N.; O'Brien, P., Synthetic approaches to two-dimensional transition metal dichalcogenide nanosheets. *Prog. Mater. Sci.* **2017,** *89*, 411-478.

38. A, P.; J, V., *Physics of crystal growth*. Cambridge University Press, 1998.

39. Kong, D.; Wang, H.; Cha, J. J.; Pasta, M.; Koski, K. J.; Yao, J.; Cui, Y., Synthesis of MoS_2 and $MoSe_2$ films with vertically aligned layers. *Nano Lett.* **2013,** *13* (3), 1341-7.

40. Sun, L.; Yuan, G.; Gao, L.; Yang, J.; Chhowalla, M.; Gharahcheshmeh, M. H.; Gleason, K. K.; Choi, Y. S.; Hong, B. H.; Liu, Z., Chemical vapour deposition. *Nat. Rev. Methods Primers* **2021,** *1* (1).

41. Choy, K. L., Chemical vapour deposition of coatings. *Prog. Mater. Sci.* **2003,** *48*, 57–170.

42. YAN, K.; FU, L.; PENG, H.; LIU, Z., Designed CVD Growth of Graphene via Process Engineering. *Acc. Chem. Res.* **2013,** *46* (10), 2263–2274.

43. van der Zande, A. M.; Huang, P. Y.; Chenet, D. A.; Berkelbach, T. C.; You, Y.; Lee, G. H.; Heinz, T. F.; Reichman, D. R.; Muller, D. A.; Hone, J. C., Grains and grain boundaries in highly crystalline monolayer molybdenum disulphide. *Nat. Mater.* **2013,** *12* (6), 554-61.

44. Najmaei, S.; Liu, Z.; Zhou, W.; Zou, X.; Shi, G.; Lei, S.; Yakobson, B. I.; Idrobo, J. C.; Ajayan, P. M.; Lou, J., Vapour phase growth and grain boundary structure of molybdenum disulphide atomic layers. *Nat. Mater.* **2013,** *12* (8), 754-9.

45. Fuchtbauer, H. G.; Tuxen, A. K.; Moses, P. G.; Topsoe, H.; Besenbacher, F.; Lauritsen, J. V., Morphology and atomic-scale structure of single-layer WS_2 nanoclusters. *Phys. Chem. Chem. Phys.* **2013,** *15* (38), 15971-80.

46. Eli´as, A. L.; pez, N. s. P.-L.; n, A. s. C.-B.; Berkdemir, A.; Lv, R.; Feng, S.; Long, A. D.; Hayashi, T.; Kim, Y. A.; Endo, M.; rrez, H. R. G.; Pradhan, N. R.; Balicas, L.; Mallouk, T. E.; pez-Urı´as, F. L.; Terrones, H.; Terrones, M., Controlled Synthesis and Transfer of Large-Area WS_2 Sheets: From Single Layer to Few Layers. *ACS Nano* **2013,** *7* (6), 5235–5242.

47. Gutierrez, H. R.; Perea-Lopez, N.; Elias, A. L.; Berkdemir, A.; Wang, B.; Lv, R.; Lopez-Urias, F.; Crespi, V. H.; Terrones, H.; Terrones, M., Extraordinary room-temperature photoluminescence in triangular WS_2 monolayers. *Nano Lett* **2013,** *13* (8), 3447-54.

48. XingliWang; Gong, Y.; Shi, G.; LeongChow, W.; Keyshar, K.; GonglanYe; RobertVajtai; Lou, J.; Liu, Z.; Ringe, E.; Tay, B. K.; Ajayan, P. M., Chemical Vapor Deposition Growth of Crystalline Monolayer $MoSe_2$. *ACS Nano* **2014,** *8* (5), 5125–5131.

49. Elı´as, A. L.; pez, N. s. P.-L.; n, A. s. C.-B.; Berkdemir, A.; Lv, R.; Feng, S.; Long, A. D.; Hayashi, T.; Kim, Y. A.; Endo, M.; rrez, H. R. G.; Pradhan, N. R.; Terrones, M., Controlled Synthesis and Transfer of Large-Area WS_2 Sheets: From Single Layer to Few Layers. *ACS Nano* **2013,** *7* (6), 5235–5242.

50. Zhang, Y.; Zhang, Y.; Ji, Q.; Ju, J.; Yuan, H.; Shi, J.; Gao, T.; Ma, D.; Liu, M.; Chen, Y.; Song, X.; Hwang, H. Y.; Cui, Y.; Liu, Z., Controlled Growth of High-Quality Monolayer WS_2 Layers on Sapphire and Imaging Its Grain Boundary. *ACS Nano* **2013,** *7* (10), 8963–8971.

51. Lin, Y. C.; Zhang, W.; Huang, J. K.; Liu, K. K.; Lee, Y. H.; Liang, C. T.; Chu, C. W.; Li, L. J., Wafer-scale MoS_2 thin layers prepared by MoO_3 sulfurization. *Nanoscale* **2012,** *4* (20), 6637-41.

52. Zhan, Y.; Liu, Z.; Najmaei, S.; Ajayan, P. M.; Lou, J., Large-area vapor-phase growth and characterization of MoS_2 atomic layers on a SiO_2 substrate. *Small* **2012,** *8* (7), 966-71.

53. Shanmugam, M.; Durcan, C. A.; Yu, B., Layered semiconductor molybdenum disulfide nanomembrane based Schottky-barrier solar cells. *Nanoscale* **2012,** *4* (23), 7399-405.

54. Tarasov, A.; Campbell, P. M.; Tsai, M.-Y.; Hesabi, Z. R.; Feirer, J.; Graham, S.; Ready, W. J.; Vogel, E. M., Highly Uniform Trilayer Molybdenum Disulfide for Wafer-Scale Device Fabrication. *Adv. Func. Mater.* **2014,** *24* (40), 6389-6400.

55. Wang, J.; Chen, L.; Lu, W.; Zeng, M.; Tan, L.; Ren, F.; Jiang, C.; Fu, L., Direct growth of molybdenum disulfide on arbitrary insulating surfaces by chemical vapor deposition. *RSC Adv.* **2015,** *5* (6), 4364-4367.

56. Song, I.; Park, C.; Hong, M.; Baik, J.; Shin, H. J.; Choi, H. C., Patternable large-scale molybdenium disulfide atomic layers grown by gold-assisted chemical vapor deposition. *Angew. Chem. Int, Ed.* **2014,** *53* (5), 1266-9.

57. Jung, Y.; Ji, E.; Capasso, A.; Lee, G.-H., Recent Progresses in the Growth of Two-dimensional Transition Metal Dichalcogenides. *J. Korean Ceram. Soc.* **2019,** *56* (1), 24-36.

58. Xia, J.; Zhu, D.; Wang, L.; Huang, B.; Huang, X.; Meng, X.-M., Large-Scale Growth of Two-Dimensional SnS_2 Crystals Driven by Screw Dislocations

and Application to Photodetectors. *Adv. Func. Mater.* **2015,** *25* (27), 4255-4261.

59. Jin, S.; Bierman, M. J.; Morin, S. A., A New Twist on Nanowire Formation: Screw-Dislocation-Driven Growth of Nanowires and Nanotubes. *The J. Phys. Chem. Lett.* **2010,** *1* (9), 1472-1480.

60. Chen, L.; Liu, B.; Abbas, A. N.; Ma, Y.; Fang, X.; Liu, Y.; Zhou, C., Screw-Dislocation-Driven Growth of Two-Dimensional Few-Layer and Pyramid-like WSe_2 by Sulfur-Assisted Chemical Vapor Deposition. *ACS Nano* **2014,** *8* (11), 11543–11551.

61. Wu, J.; Hu, Z.; Jin, Z.; Lei, S.; Guo, H.; Chatterjee, K.; Zhang, J.; Yang, Y.; Li, B.; Liu, Y.; Lai, J.; Vajtai, R.; Yakobson, B.; Tang, M.; Lou, J.; Ajayan, P. M., Spiral Growth of $SnSe_2$ Crystals by Chemical Vapor Deposition. *Adv. Mater. Interfaces* **2016,** *3* (16).

62. Zhang, Y.; Ji, Q.; Wen, J.; Li, J.; Li, C.; Shi, J.; Zhou, X.; Shi, K.; Chen, H.; Li, Y.; Deng, S.; Xu, N.; Liu, Z.; Zhang, Y., Monolayer MoS_2 Dendrites on a Symmetry-Disparate $SrTiO_3$ (001) Substrate: Formation Mechanism and Interface Interaction. *Adv. Func. Mater.* **2016,** *26* (19), 3299-3305.

63. AJ, M., *Energy Diagram for Crystallization*. University of Cambridge, 1999.

64. Cubillas, P.; Anderson, M. W., Synthesis Mechanism: Crystal Growth and Nucleation. In *Zeolites and Catalysis*, 2010; pp 1-55.

65. Wang, Q. H.; Kalantar-Zadeh, K.; Kis, A.; Coleman, J. N.; Strano, M. S., Electronics and optoelectronics of two-dimensional transition metal dichalcogenides. *Nat. Nanotechnol.* **2012,** *7* (11), 699-712.

66. Geim, A. K.; Grigorieva, I. V., Van der Waals heterostructures. *Nature* **2013,** *499* (7459), 419-25.

67. Fiori, G.; Bonaccorso, F.; Iannaccone, G.; Palacios, T.; Neumaier, D.; Seabaugh, A.; Banerjee, S. K.; Colombo, L, Electronics based on two-dimensional materials. *Nat. Nanotechnol.* **2014,** *9* (10), 768-79.

68. Jariwala, D.; Sangwan, V. K.; Lauhon, L. J.; Marks, T. J.; Hersam, M. C., Emerging Device Applications for Semiconducting Two-Dimensional Transition Metal Dichalcogenides. *ACS Nano* **2014,** *8* (2), 1102–1120.

69. Zhang, H., Ultrathin Two-Dimensional Nanomaterials. *ACS Nano* **2015,** *9* (10), 9451–9469.

70. Miller, J. R.; Simon, P., Electrochemical Capacitors for Energy Management. *Science* **2008,** *321*, 651-652.

71. millo, T. F. J.; Jorgensen, K. P.; Bonde, J.; Nielsen, J. H.; Horch, S.; Chorkendorff, I., Identification of Active Edge Sites for Electrochemical H_2 Evolution from MoS_2 Nanocatalyst. *Science* **2007,** *317*, 100-102.

72. Lukowski, M. A.; Daniel, A. S.; Meng, F.; Forticaux, A.; Li, L.; Jin, S., Enhanced hydrogen evolution catalysis from chemically exfoliated metallic MoS_2 nanosheets. *J. Am. Chem. Soc.* **2013,** *135* (28), 10274-7.

73. Xie, J.; Zhang, H.; Li, S.; Wang, R.; Sun, X.; Zhou, M.; Zhou, J.; Lou, X. W.; Xie, Y., Defect-rich MoS_2 ultrathin nanosheets with additional active edge sites for enhanced electrocatalytic hydrogen evolution. *Adv. Mater.* **2013,** *25* (40), 5807-13.

74. Voiry, D.; Salehi, M.; Silva, R.; Fujita, T.; Chen, M.; Asefa, T.; Shenoy, V. B.; Eda, G.; Chhowalla, M., Conducting MoS_2 nanosheets as catalysts for hydrogen evolution reaction. *Nano Lett.* **2013,** *13* (12), 6222-7.

75. Xie, J.; Zhang, J.; Li, S.; Grote, F.; Zhang, X.; Zhang, H.; Wang, R.; Lei, Y.; Pan, B.; Xie, Y., Controllable disorder engineering in oxygen-incorporated MoS_2 ultrathin nanosheets for efficient hydrogen evolution. *J. Am. Chem. Soc.* **2013,** *135* (47), 17881-8.

76. Yu, Y.; Huang, S. Y.; Li, Y.; Steinmann, S. N.; Yang, W.; Cao, L., Layer-dependent electrocatalysis of MoS_2 for hydrogen evolution. *Nano Lett.* **2014,** *14* (2), 553-8.

77. Gupta, A.; Sakthivel, T.; Seal, S., Recent development in 2D materials beyond graphene. *Prog. Mater. Sci.* **2015,** *73*, 44-126.

78. Chhowalla, M.; Jena, D.; Zhang, H., Two-dimensional semiconductors for transistors. *Nat. Rev. Mater.* **2016,** *1*, 1-15.

79. Eknapakul, T.; King, P. D.; Asakawa, M.; Buaphet, P.; He, R. H.; Mo, S. K.; Takagi, H.; Shen, K. M.; Baumberger, F.; Sasagawa, T.; Jungthawan, S.; Meevasana, W., Electronic structure of a quasi-freestanding MoS_2 monolayer. *Nano Lett.* **2014,** *14* (3), 1312-6.

80. Böker, T.; Severin, R.; Müller, A.; Janowitz, C.; Manzke, R.; Voß, D.; Krüger, P.; Mazur, A.; Pollmann, J., Band structure of MoS_2,$MoSe_2$,and α−$MoTe_2$:Angle-resolved photoelectron spectroscopy andab initiocalculations. *Phys. Rev. B* **2001,** *64* (23).

81. Saigal, N.; Ghosh, S., Evidence for two distinct defect related luminescence features in monolayer MoS_2. *Appl. Phys. Lett.* **2016,** *109* (12).

82. Yu, Z. G.; Zhang, Y. W.; Yakobson, B. I., An Anomalous Formation

Pathway for Dislocation-Sulfur Vacancy Complexes in Polycrystalline Monolayer MoS_2. *Nano Lett.* **2015,** *15* (10), 6855-61.

83. Coy Diaz, H.; Addou, R.; Batzill, M., Interface properties of CVD grown graphene transferred onto MoS_2(0001). *Nanoscale* **2014,** *6* (2), 1071-8.

84. Shen, P.-C.; Lin, Y.; Su, C.; McGahan, C.; Lu, A.-Y.; Ji, X.; Wang, X.; Wang, H.; Mao, N.; Guo, Y.; Park, J.-H.; Wang, Y.; Tisdale, W.; Li, J.; Ling, X.; Aidala, K. E.; Palacios, T.; Kong, J., Healing of donor defect states in monolayer molybdenum disulfide using oxygen-incorporated chemical vapour deposition. *Nat. Electron.* **2021,** *5* (1), 28-36.

85. Radisavljevic, B.; Radenovic, A.; Brivio, J.; Giacometti, V.; Kis, A., Single-layer MoS_2 transistors. *Nat. Nanotechnol.* **2011,** *6* (3), 147-50.

86. Butler, S. Z.; Hollen, S. M.; Linyou Cao, Y. C.; Gupta, J. A.; rrez, H. R. G.; Heinz, T. F.; Hong, S. S.; Huang, J.; Ismach, A. F.; Johnston-Halperin, E.; Kuno, M.; Plashnitsa, V. V.; Robinson, R. D.; Ruoff, R. S.; Salahuddin, S.; Shan, J.; Shi, L.; Spencer, O. M. G.; Terrones, M.; Windl, W.; Goldberger, J. E., Progress, Challenges, and Opportunities in Two-Dimensional Materials Beyond Graphene. *ACS Nano* **2013,** *7* (4), 2898–2926.

87. Mak, K. F.; Shan, J., Photonics and optoelectronics of 2D semiconductor transition metal dichalcogenides. *Nat. Photon.* **2016,** *10* (4), 216-226.

88. Toh, R. J.; Sofer, Z.; Luxa, J.; Sedmidubsky, D.; Pumera, M., 3R phase of MoS_2 and WS_2 outperforms the corresponding 2H phase for hydrogen evolution. *Chem. Commun.* **2017,** *53* (21), 3054-3057.

89. Zhang, W.; Wu, J., Stacking order and driving forces in the layered charge density wave phase of 1T-MX_2 (M = Nb, Ta and X = S, Se). *Mater. Res. Express* **2023,** *10* (4).

90. Rosenberger, M. R.; Chuang, H. J.; Phillips, M.; Oleshko, V. P.; McCreary, K. M.; Sivaram, S. V.; Hellberg, C. S.; Jonker, B. T., Twist Angle-Dependent Atomic Reconstruction and Moire Patterns in Transition Metal Dichalcogenide Heterostructures. *ACS Nano* **2020,** *14* (4), 4550-4558.

91. Woods, C. R.; Ares, P.; Nevison-Andrews, H.; Holwill, M. J.; Fabregas, R.; Guinea, F.; Geim, A. K.; Novoselov, K. S.; Walet, N. R.; Fumagalli, L., Charge-polarized interfacial superlattices in marginally twisted hexagonal boron nitride. *Nat. Commun.* **2021,** *12* (1), 347.

92. Weston, A.; Zou, Y.; Enaldiev, V.; Summerfield, A.; Clark, N.; Zolyomi, V.; Graham, A.; Yelgel, C.; Magorrian, S.; Zhou, M.; Zultak, J.; Hopkinson, D.; Barinov, A.; Bointon, T. H.; Kretinin, A.; Wilson, N. R.; Beton,

P. H.; Fal'ko, V. I.; Haigh, S. J.; Gorbachev, R., Atomic reconstruction in twisted bilayers of transition metal dichalcogenides. *Nat. Nanotechnol.* **2020,** *15* (7), 592-597.

93. Berkdemir, A.; Gutiérrez, H. R.; Botello-Méndez, A. R.; Perea-López, N.; Elías, A. L.; Chia, C.-I.; Wang, B.; Crespi, V. H.; López-Urías, F.; Charlier, J.-C.; Terrones, H.; Terrones, M., Identification of individual and few layers of WS_2 using Raman Spectroscopy. *Sci. Rep.* **2013,** *3* (1).

94. Liu, B.; Fathi, M.; Chen, L.; Abbas, A.; Ma, Y.; Zhou, C., Chemical Vapor Deposition Growth of Monolayer WSe_2 with Tunable Device Characteristics and Growth Mechanism Study. *ACS Nano* **2015,** *9* (6), 6119–6127.

95. Zhao, M.; Ye, Z.; Suzuki, R.; Ye, Y.; Zhu, H.; Xiao, J.; Wang, Y.; Iwasa, Y.; Zhang, X., Atomically phase-matched second-harmonic generation in a 2D crystal. *Light. Sci. Appl.* **2016,** *5* (8), e16131.

96. Liu, K.; Zhang, L.; Cao, T.; Jin, C.; Qiu, D.; Zhou, Q.; Zettl, A.; Yang, P.; Louie, S. G.; Wang, F., Evolution of interlayer coupling in twisted molybdenum disulfide bilayers. *Nat. Commun.* **2014,** *5*, 4966.

97. Mandal, D.; Routh, P.; Nandi, A. K., A New Facile Synthesis of Tungsten Oxide from Tungsten Disulfide: Structure Dependent Supercapacitor and Negative Differential Resistance Properties. *Small* **2018,** *14* (4).

98. Shirazi, M.; Kessels, W. M. M.; Bol, A. A., Initial stage of atomic layer deposition of 2D-MoS_2 on a SiO_2 surface: a DFT study. *Phys. Chem. Chem. Phys.* **2018,** *20* (24), 16861-16875.

99. Suzuki, H.; Kishibuchi, M.; Misawa, M.; Shimogami, K.; Ochiai, S.; Kokura, T.; Liu, Y.; Hashimoto, R.; Liu, Z.; Tsuruta, K.; Miyata, Y.; Hayashi, Y., Self-Limiting Growth of Monolayer Tungsten Disulfide Nanoribbons on Tungsten Oxide Nanowires. *ACS Nano* **2023,** *17* (10), 9455-9467.

100. Jung, Y.; Ryu, H.; Kim, H.; Moon, D.; Joo, J.; Hong, S. C.; Kim, J.; Lee, G. H., Nucleation and Growth of Monolayer MoS_2 at Multisteps of MoO_2 Crystals by Sulfurization. *ACS Nano* **2023,** *17* (8), 7865-7871.

101. Jiang, D.; Wang, X.; Chen, R.; Sun, J.; Kang, H.; Ji, D.; Liu, Y.; Wei, D., Self-Expanding Molten Salt-Driven Growth of Patterned Transition-Metal Dichalcogenide Crystals. *J. Am. Chem. Soc.* **2022,** *144* (19), 8746-8755.

102. Chow, P. K.; Singh, E.; Viana, B. C.; Gao, J.; Luo, J.; Li, J.; Lin, Z.; Elı´as, A. L.; Shi, Y.; Wang, Z.; Terrones, M.; Koratkar, N., Wetting of Mono and Few-Layered WS_2 and MoS_2 Films Supported on Si/SiO_2 Substrates. *ACS Nano* **2015,** *9* (3), 3023–3031.

103. Brochará, F., Motions of Droplets on Solid Surfaces Induced by Chemical or Thermal Gradients. *Langmuir* **1989,** *5*, 432-438.

104. Xu, X.; Yao, W.; Xiao, D.; Heinz, T. F., Spin and pseudospins in layered transition metal dichalcogenides. *Nat. Phys.* **2014,** *10* (5), 343-350.

105. Sie, E. J.; McIver, J. W.; Lee, Y. H.; Fu, L.; Kong, J.; Gedik, N., Valley-selective optical Stark effect in monolayer WS_2. *Nat. Mater.* **2015,** *14* (3), 290-4.

106. Mak, K. F.; McGill, K. L.; Park, J.; McEuen, P. L., The valley Hall effect in MoS_2 transistors. *Science* **2014,** *344* (6191).

107. Wu, W.; Wang, L.; Li, Y.; Zhang, F.; Lin, L.; Niu, S.; Chenet, D.; Zhang, X.; Hao, Y.; Heinz, T. F.; Hone, J.; Wang, Z. L., Piezoelectricity of single-atomic-layer MoS_2 for energy conversion and piezotronics. *Nature* **2014,** *514* (7523), 470-4.

108. Ye, Z.; Cao, T.; O'Brien, K.; Zhu, H.; Yin, X.; Wang, Y.; Louie, S. G.; Zhang, X., Probing excitonic dark states in single-layer tungsten disulphide. *Nature* **2014,** *513* (7517), 214-8.

109. Robert, C.; Lagarde, D.; Cadiz, F.; Wang, G.; Lassagne, B.; Amand, T.; Balocchi, A.; Renucci, P.; Tongay, S.; Urbaszek, B.; Marie, X., Exciton radiative lifetime in transition metal dichalcogenide monolayers. *Phys. Rev. B* **2016,** *93* (20).

110. Akinwande, D.; Huyghebaert, C.; Wang, C. H.; Serna, M. I.; Goossens, S.; Li, L. J.; Wong, H. P.; Koppens, F. H. L., Graphene and two-dimensional materials for silicon technology. *Nature* **2019,** *573* (7775), 507-518.

111. Serrao, C. R.; Diamond, A. M.; Hsu, S.-L.; You, L.; Gadgil, S.; Clarkson, J.; Carraro, C.; Maboudian, R.; Hu, C.; Salahuddin, S., Highly crystalline MoS_2 thin films grown by pulsed laser deposition. *Appl. Phys. Lett.* **2015,** *106* (5).

112. Serna, M. I.; Yoo, S. H.; Moreno, S.; Xi, Y.; Oviedo, J. P.; Choi, H.; Alshareef, H. N.; Kim, M. J.; Minary-Jolandan, M.; Quevedo-Lopez, M. A., Large-Area Deposition of MoS_2 by Pulsed Laser Deposition with In Situ Thickness Control. *ACS Nano* **2016,** *10* (6), 6054-61.

113. Tumino, F.; Casari, C. S.; Passoni, M.; Russo, V.; Li Bassi, A., Pulsed laser deposition of single-layer MoS_2 on Au(111): from nanosized crystals to large-area films. *Nanoscale Adv.* **2019,** *1* (2), 643-655.

114. Tan, L. K.; Liu, B.; Teng, J. H.; Guo, S.; Low, H. Y.; Tan, H. R.; Chong, C. Y.; Yang, R. B.; Loh, K. P., Atomic layer deposition of a MoS_2 film. *Nanoscale* **2014,** *6* (18), 10584-8.

115. Richey, N. E.; de Paula, C.; Bent, S. F., Understanding chemical and physical mechanisms in atomic layer deposition. *J. Chem. Phys.* **2020,** *152* (4), 040902.
116. Kim, D. H.; Park, J. C.; Park, J.; Cho, D.-Y.; Kim, W.-H.; Shong, B.; Ahn, J.-H.; Park, T. J., Wafer-Scale Growth of a MoS_2 Monolayer via One Cycle of Atomic Layer Deposition: An Adsorbate Control Method. *Chem. Mater.* **2021,** *33* (11), 4099-4105.
117. Shi, J.; Zhang, X.; DonglinMa; Zhu, J.; YuZhang; Guo, Z.; YuYao; Ji, Q.; Song, X.; Zhang, Y.; Li, C.; Liu, Z.; Zhu, W.; Zhang, Y., Substrate Facet Effect on the Growth of Monolayer MoS_2 on Au Foils. *ACS Nano* **2015,** *9* (4), 4017–4025.
118. Kang, K.; Xie, S.; Huang, L.; Han, Y.; Huang, P. Y.; Mak, K. F.; Kim, C. J.; Muller, D.; Park, J., High-mobility three-atom-thick semiconducting films with wafer-scale homogeneity. *Nature* **2015,** *520* (7549), 656-60.
119. Kim, H.; Ovchinnikov, D.; Deiana, D.; Unuchek, D.; Kis, A., Suppressing Nucleation in Metal-Organic Chemical Vapor Deposition of MoS_2 Monolayers by Alkali Metal Halides. *Nano Lett.* **2017,** *17* (8), 5056-5063.
120. Chiappe, D.; Mongillo, M.; Asselberghs, I.; Kazzi, S. E.; Caymax, M.; Barla, K.; De Gendt, S.; Radu, I.; Huyghebaert, C., Demonstration of Direction Dependent Conduction through MoS_2 Films Prepared by Tunable Mass Transport Fabrication. *ECS J. Solid State Sci. Technol.* **2016,** *5* (11), Q3046-Q3049.
121. Cho, D. H.; Lee, W. J.; Wi, J. H.; Han, W. S.; Yun, S. J.; Shin, B.; Chung, Y. D., Enhanced sulfurization reaction of molybdenum using a thermal cracker for forming two-dimensional MoS_2 layers. *Phys. Chem. Chem. Phys.* **2018,** *20* (23), 16193-16201.
122. Taheri, P.; Wang, J.; Xing, H.; Destino, J. F.; Arik, M. M.; Zhao, C.; Kang, K.; Blizzard, B.; Zhang, L.; Zhao, P.; Huang, S.; Yang, S.; Bright, F. V.; Cerne, J.; Zeng, H., Growth mechanism of largescale MoS_2 monolayer by sulfurization of MoO_3 film. *Mater. Res. Express* **2016,** *3* (7).
123. Romanov, R. I.; Kozodaev, M. G.; Myakota, D. I.; Chernikova, A. G.; Novikov, S. M.; Volkov, V. S.; Slavich, A. S.; Zarubin, S. S.; Chizhov, P. S.; Khakimov, R. R.; Chouprik, A. A.; Hwang, C. S.; Markeev, A. M., Synthesis of Large Area Two-Dimensional MoS_2 Films by Sulfurization of Atomic Layer Deposited MoO_3 Thin Film for Nanoelectronic Applications. *ACS Appl. Nano Mater.* **2019,** *2* (12), 7521-7531.
124. Nikam, R. D.; Lu, A. Y.; Sonawane, P. A.; Kumar, U. R.; Yadav, K.; Li,

L. J.; Chen, Y. T., Three-Dimensional Heterostructures of MoS_2 Nanosheets on Conducting MoO_2 as an Efficient Electrocatalyst To Enhance Hydrogen Evolution Reaction. *ACS Appl. Mater. Interfaces* **2015,** *7* (41), 23328-35.

125. Pu, E.; Liu, D.; Ren, P.; Zhou, W.; Tang, D.; Xiang, B.; Wang, Y.; Miao, J., Ultrathin MoO2 nanosheets with good thermal stability and high conductivity. *AIP Adv.* **2017,** *7* (2).

126. Lawrence, G. M., Hex-square moire patterns in imagers using microchannel plates. *Appl. Opt.* **1989,** *28* (20), 4337-4343.

127. Shang, S. L.; Lindwall, G.; Wang, Y.; Redwing, J. M.; Anderson, T.; Liu, Z. K., Lateral Versus Vertical Growth of Two-Dimensional Layered Transition-Metal Dichalcogenides: Thermodynamic Insight into MoS_2. *Nano Lett.* **2016,** *16* (9), 5742-50.

128. Ye, H.; Zhou, J.; Er, D.; Price, C. C.; Yu, Z.; Liu, Y.; Lowengrub, J.; Lou, J.; Liu, Z.; Shenoy, V. B., Toward a Mechanistic Understanding of Vertical Growth of van der Waals Stacked 2D Materials: A Multiscale Model and Experiments. *ACS Nano* **2017,** *11* (12), 12780-12788.

129. Aljarb, A.; Fu, J. H.; Hsu, C. C.; Chuu, C. P.; Wan, Y.; Hakami, M.; Naphade, D. R.; Yengel, E.; Lee, C. J.; Brems, S.; Chen, T. A.; Li, M. Y.; Bae, S. H.; Hsu, W. T.; Cao, Z.; Albaridy, R.; Lopatin, S.; Chang, W. H.; Anthopoulos, T. D.; Kim, J.; Li, L. J.; Tung, V., Ledge-directed epitaxy of continuously self-aligned single-crystalline nanoribbons of transition metal dichalcogenides. *Nat. Mater.* **2020,** *19* (12), 1300-1306.

130. Dahl-Petersen, C.; Saric, M.; Brorson, M.; Moses, P. G.; Rossmeisl, J.; Lauritsen, J. V.; Helveg, S., Topotactic Growth of Edge-Terminated MoS_2 from MoO_2 Nanocrystals. *ACS Nano* **2018,** *12* (6), 5351-5358.

131. Liang, L.; Meunier, V., First-principles Raman spectra of MoS_2, WS_2 and their heterostructures. *Nanoscale* **2014,** *6* (10), 5394-401.

132. Rao, R.; Islam, A. E.; Singh, S.; Berry, R.; Kawakami, R. K.; Maruyama, B.; Katoch, J., Spectroscopic evaluation of charge-transfer doping and strain in graphene/MoS_2 heterostructures. *Phys. Rev. B* **2019,** *99* (19).

133. Zhang, X.; Shao, Z.; Zhang, X.; He, Y.; Jie, J., Surface Charge Transfer Doping of Low-Dimensional Nanostructures toward High-Performance Nanodevices. *Adv. Mater.* **2016,** *28* (47), 10409-10442.

134. Bhanu, U.; Islam, M. R.; Tetard, L.; Khondaker, S. I., Photoluminescence quenching in gold - MoS_2 hybrid nanoflakes. *Sci. Rep.* **2014,**

4, 5575.

135. Kim, I. S.; Sangwan, V. K.; Jariwala, D.; Wood, J. D.; Park, S.; Chen, K.-S.; Shi, F.; Ruiz-Zepeda, F.; Ponce, A.; Jose-Yacaman, M.; Dravid, V. P.; Marks, T. J.; Hersam, M. C.; Lauhon, L. J., Influence of Stoichiometry on the Optical and Electrical Properties of Chemical Vapor Deposition Derived MoS_2. *ACS Nano* **2014,** *8* (10), 10551–10558.

136. Sangwan, V. K.; Jariwala, D.; Kim, I. S.; Chen, K. S.; Marks, T. J.; Lauhon, L. J.; Hersam, M. C., Gate-tunable memristive phenomena mediated by grain boundaries in single-layer MoS_2. *Nat. Nanotechnol.* **2015,** *10* (5), 403-6.

137. Su, L.; Zhang, Y.; Yu, Y.; Cao, L., Dependence of coupling of quasi 2-D MoS_2 with substrates on substrate types, probed by temperature dependent Raman scattering. *Nanoscale* **2014,** *6* (9), 4920-7.

138. Velicky, M.; Rodriguez, A.; Bousa, M.; Krayev, A. V.; Vondracek, M.; Honolka, J.; Ahmadi, M.; Donnelly, G. E.; Huang, F.; Abruna, H. D.; Novoselov, K. S.; Frank, O., Strain and Charge Doping Fingerprints of the Strong Interaction between Monolayer MoS_2 and Gold. *J. Phys. Chem. Lett.* **2020,** *11* (15), 6112-6118.

Abstract in Korean (국문 초록)

금속 전구체와 성장 촉진제를 통한 전이금속 칼코겐화물의 성장 제어

정연준

공과대학 재료공학부

서울대학교

2차원(2D) 재료와 그 이종 구조는 차세대 광전자, 스핀트로닉스, 밸리트로닉스 및 전자공학 분야에서 유망한 분야입니다. 최근 2D 소재의 다양한 성장 연구가 진전되고 있지만, 2D 소재의 성장 과정에서 원하는 모양과 품질로 소재 성장을 정밀하게 제어하고 단일 도메인을 합성하는 것이 어렵기 때문에 고품질 2D 소재를 얻기 위해서는 여전히 벌크 크리스탈을 기계적으로 박리하는 방법이 가장 많이 사용되고 있습니다.

본 논문에서는 2D 전이금속 디칼코게나이드 소재의 물성을 조절하기 위한 성장 및 성장 메커니즘에 대한 연구를 진행하였습니다. 자세한 연구를 소개하기에 앞서 1장에서는 성장 메커니즘 분석의 중요성을 포함하여 2D 전이금속 칼코겐화물 소재의 물성 및 성장에 대한 간략한 일반적 배경을 설명합니다. 2장에서는 기존의 합성법에서의 문제점을 개선한 세 가지 방식의 서로다른 전이금속 디칼코게나이드의 성장법을 설명합니다.

첫번째는 성장촉진제를 이용하여 MoS_2를 성장시키고 성장시킨 MoS_2의 PL을 ex-situ로 강화했습니다. PL 이미징을 통해 반복적인 빛 조명으로 인해 이미징 영역 내에서 PL 강도가 점진적으로 향상되는 것을 관찰했습니다. 포인트 PL 측정은 PL 강도가 약 7배 향상되었다는 정량적 증거를 제공했습니다. 그리고 저온 PL 및 XPS 측정은 이런 광학적특성의 강화가 결함 치유와 관계가 있음을 보여줍니다. 따라서 이러한 향

상은 엑시톤의 형성 및 직접밴드갭을 통핸 발광 결합 경로의 증가와 반복적인 빛 조명에 의해 촉진된 결함 치유에 의한 것입니다.

두번째로 성장 과정에서 생성되는 중간상인 액상 텅스텐 산화물(WO_x)이 다층 WS_2의 성장을 촉진하는 것을 확인하였습니다. 높은 산소비(x>3)를 갖는 중간상 WO_x는 액상이 되어 황이 액상 WO_x에 용해될 수 있고, 그 결과 WO_x 표면에 다층 WS_2가 핵을 형성하게 됩니다. 그런 다음 WS_2와 WO_x 사이의 높은 계면 에너지로 인해 WS_2가 액체 WO_x를 바깥쪽으로 밀어내면서 옆으로 성장합니다. 성장한 다층 WS_2 단결정은 2H 및 3R의 다양한 적층 순서를 가지며, 이는 2차 고조파 생성(SHG) 신호와 광발광(PL)으로 확인했습니다.

마지막으로, 저는 고품질의 패싯 MoO_2 결정을 황화하여 단층 MoS_2의 핵 형성 및 성장 거동을 확인하였습니다. MoS_2 층은 MoO_2 결정의 테라스 위치에서 핵을 형성하고 MoO_2 표면에 대한 결정 상관 관계와 함께 에피택셜로 성장했습니다. 에피택셜로 성장한 MoS_2 층은 SiO_2 기판에서 바깥쪽으로 팽창하여 단층 단결정 필름을 형성하지만, 여러 테라스 위치로 인해 MoO_2 표면에서 MoS_2 층이 여러 번 핵 형성됨에도 불구하고 가장 넓게 노출되어있는 MoO_2 표면에서 성장한 MoS_2만이 단층 단결정 필름을 형성합니다. MoS_2와 금속 MoO_2 사이의 효율적인 전하 이동으로 인해 MoS_2의 광발광이 퀀칭되고, SiO_2 기판으로 뻗어 나온 MoS_2는 (15 cm^2V-1s-1)의 높은 캐리어 이동도를 보여, MoO_2 결정을 시드 및 전구체로 사용하여 고품질의 단층 MoS_2 필름을 성장시킬 수 있음을 나타냅니다. 우리의 연구는 패싯 MoO_2 결정을 사용하여 고품질 MoS_2를 성장시키는 경로를 보여주고 계단 모양의 표면에서 2D 재료의 핵 형성 및 성장에 대한 더 깊은 이해를 제공합니다.

우리의 연구 결과는 2D 재료의 성장에 대한 더 나은 이해를 제공하여 2D 재료의 새로운 성장 방법을 설계하는 데 적용될 수 있습니다.

Keywords : 2차원 나노물질, 전이금속 칼코겐화물, 성장 메커니즘, 화학기상증착법, 물리기상증착법, 칼코겐화

Student Number : 2020-28958